

# Structural, Vibrational, and Elastic Properties of Yttrium Orthoaluminate Nanoperovskite at High Pressures

M. A. Hernández-Rodríguez,<sup>\*,†,‡</sup> V. Monteseguro,<sup>#</sup> A. D. Lozano-Gorrín,<sup>†</sup> F. J. Manjón,<sup>⊥</sup>  
J. González-Platas,<sup>∇</sup> P. Rodríguez-Hernández,<sup>†,‡,||</sup> A. Muñoz,<sup>†,‡,||</sup> V. Lavín,<sup>†,‡,§</sup> I. R. Martín,<sup>†,‡,||</sup>  
and U. R. Rodríguez-Mendoza<sup>†,‡,||</sup>

<sup>†</sup>Departamento de Física, Universidad de La Laguna, Apdo. 456. E-38200 San Cristóbal de La Laguna, Santa Cruz de Tenerife, Spain

<sup>‡</sup>MALTA Consolider Team, Universidad de La Laguna, Apdo. 456. E-38200 San Cristóbal de La Laguna, Santa Cruz de Tenerife, Spain

<sup>§</sup>Instituto Universitario de Estudios Avanzados en Física Atómica, Molecular y Fotónica (IUdEA), Universidad de La Laguna, Apdo. 456. E-38200 San Cristóbal de La Laguna, Santa Cruz de Tenerife, Spain

<sup>||</sup>Instituto Universitario de Materiales y Nanotecnología (IMN), Apdo. 456. Universidad de La Laguna, E-38200 San Cristóbal de La Laguna, Santa Cruz de Tenerife, Spain

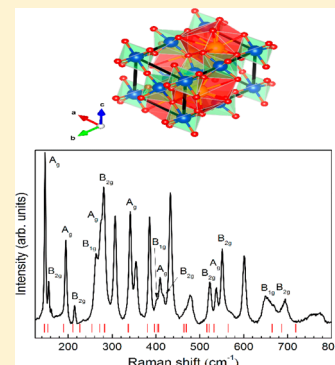
<sup>⊥</sup>Instituto de Diseño para la Fabricación y Producción Automatizada, MALTA Consolider Team, Universitat Politècnica de València, Cno. de Vera s/n, 46022 Valencia, Spain

<sup>#</sup>Beamlines BM23 & ID24, European Synchrotron Radiation Facility, 38043 Grenoble, France

<sup>∇</sup>Servicio de Difracción de Rayos X (SIDIX), Departamento de Física, Universidad de La Laguna, Apdo. 456. E-38200 San Cristóbal de La Laguna, Santa Cruz de Tenerife, Spain

## Supporting Information

**ABSTRACT:** The structural and vibrational properties of nanocrystalline yttrium orthoaluminate perovskite ( $\text{YAlO}_3$ ) under compression have been experimentally studied. Experimental results have been compared to *ab initio* simulations of bulk  $\text{YAlO}_3$  in the framework of the density functional theory. Furthermore, they have been complemented with an *ab initio* study of its elastic properties at different pressures. Calculated total and partial phonon density of states have allowed us to understand the contribution of the different atoms and structural units,  $\text{YO}_{12}$  dodecahedra and  $\text{AlO}_6$  octahedra, to the vibrational modes. The calculated infrared-active modes and their pressure dependence are also reported. Finally, the pressure dependences of the elastic constants and the mechanical stability of the perovskite structure have been analyzed in detail, showing that this phase is mechanically stable until 92 GPa. In fact, experimental results up to 30 GPa show no evidence of any phase transition. A previously proposed possible phase transition in  $\text{YAlO}_3$  above 80 GPa is also discussed.



## 1. INTRODUCTION

Perovskites have been intensively researched due to their relevance from both the viewpoint of fundamental physics and device applications. In particular,  $\text{ABO}_3$ -type perovskite oxides, where A and B denote two different cations, have gained interest for their potential use in oxide-based electronics, due to their fascinating and multifunctional electronic properties beyond conventional semiconductors. Notably, most perovskite oxides are wide band gap semiconductors and show exceptional optical properties, which are employed for optoelectronic devices as nonlinear optical crystals,<sup>1,2</sup> scintillators,<sup>3</sup> photoluminescence and electroluminescence materials,<sup>4,5</sup> as well as solar cells.<sup>6</sup> In particular, perovskites can be found in several applications as optical sensors when they are doped with rare earth ions. For instance, optical temperature sensors are based on  $\text{Na}_{0.5}\text{Bi}_{0.5}\text{TiO}_3$  doped with  $\text{Er}^{3+}$  or codoped with  $\text{Er}^{3+}/\text{Yb}^{3+}$ ,<sup>7,8</sup> and also on  $\text{BaTiO}_3$  doped with  $\text{Er}^{3+}$ .<sup>9</sup> Among all perovskites, yttrium orthoaluminate perovskite ( $\text{YAlO}_3$ ) has

shown excellent physical and chemical properties, such as high hardness, good structural stability, and large mechanical strength, which make it an excellent candidate as a laser host material for lanthanide ions.<sup>10–14</sup>

Research in nanomaterials has attracted the interest of scientists from several fields due to their unique properties,<sup>15</sup> being one of their main advantages that they keep the bulk counterpart properties for sizes larger than 10–20 nm. The interest in rare-earth-doped nanoperovskites is based on the fact that the chemistry and optical spectroscopy of the analogous perovskite bulk crystals are well-known, opening the possibility to establish meaningful comparisons between the properties of the nanosized and bulk materials. In this regard, several works focused on studies of the properties of rare-earth-

Received: May 4, 2017

Revised: June 23, 2017

Published: June 24, 2017

doped nanoperovskites have been carried out.<sup>16–20</sup> Among interesting applications of nanoperovskites, we can cite their use as optical thermal sensors,<sup>7–9,21</sup> CO sensors,<sup>22</sup> and single photon emitters.<sup>23</sup>

Due to the numerous practical applications of perovskites, the study and understanding of their properties becomes an essential necessity. Especially, the knowledge of their elastic properties and mechanical stability at high pressure (HP) is a relevant subject that can also provide interesting information on their possible structural transformations through the stability criteria. On the other hand, since phonons play an important role in the electrical, thermal, and optical properties of materials, it is necessary to understand its lattice dynamics in order to go deeper into the physical properties of these compounds.

HP experiments in materials allow one to access interesting information just varying the interatomic distance and bonds. In this sense, the HP study of perovskites could provide a better understanding of possible changes occurring in their structural and vibrational properties and, hence, to understand possible changes of their luminescence properties when perovskites are doped, for instance, with rare earth ions. In particular, a number of experimental and theoretical HP studies have been performed in  $\text{AAIO}_3$  ( $A = \text{Sc}, \text{Y}, \text{Gd}, \text{Pr}, \text{Nd}, \text{La}, \dots$ ) perovskites,<sup>24–32</sup> and in particular, joint HP studies of the structural and vibrational properties have been reported for  $\text{LaAlO}_3$  and  $\text{PrAlO}_3$ .<sup>33,34</sup> In fact, a model to predict the structural behavior of perovskites at HP has been reported.<sup>35</sup> As regards  $\text{YAlO}_3$ , the pressure dependence of the fluorescence emission of  $\text{Nd}^{3+}$ ,  $\text{Cr}^{3+}$ , and  $\text{Mn}^{4+}$  ions in  $\text{YAlO}_3$  has already been studied.<sup>36–38</sup> However, the studies of the elastic properties of  $\text{YAlO}_3$  and several perovskites ( $\text{SmAlO}_3$ ,  $\text{GdAlO}_3$ , and  $\text{ScAlO}_3$ ) have only been analyzed at ambient pressure,<sup>39,40</sup> with the elastic properties of  $\text{ScAlO}_3$  perovskite being the only ones studied at HP to our knowledge.<sup>41,42</sup>

In this work, we report an extensive study of the structural, vibrational, and elastic properties of bulk and nanoscaled  $\text{YAlO}_3$  perovskite at HP. Experimental X-ray diffraction (XRD) and Raman scattering (RS) measurements of the  $\text{YAlO}_3$  nanoperovskite (with sizes around 40 nm) at HP have been compared to previously reported experimental and theoretical data of the bulk counterpart,<sup>25,26,29</sup> and with our *ab initio* calculations for bulk  $\text{YAlO}_3$ . Finally, the pressure dependence of the elastic constants and the HP mechanical stability of the  $\text{YAlO}_3$  perovskite, including a possible phase transition above 80 GPa previously proposed,<sup>29</sup> is reported and discussed.

## 2. EXPERIMENTAL DETAILS

Nanocrystalline  $\text{YAlO}_3$  was successfully synthesized by the Pechini citrate sol–gel method in air atmosphere.<sup>43</sup> Stoichiometric molar ratios of high-purity  $\text{Y}(\text{NO}_3)_3 \cdot 4\text{H}_2\text{O}$  (Aldrich, 99.9%) and  $\text{Al}(\text{NO}_3)_3 \cdot 9\text{H}_2\text{O}$  (Aldrich, 99.9%) materials were dissolved in 25 mL of 1 M  $\text{HNO}_3$  under stirring at 80 °C (353 K) for 3 h. Then, citric acid, with a molar ratio of metal ions to citric acid of 1:2, was added to the solution, which was stirred and heated at 90 °C (363 K) until reaching the transparency of the solution. Then, 4 mg of polyethylene glycol was added to the solution. This last step created a gel that was fired at 400 °C (673 K) for 6 h in order to remove the residual nitrates and organic compounds. The subsequently obtained powder sample was burnt out at 1200 °C (1473 K) for 20 h, and finally, a second thermal treatment was performed at 1550 °C (1823 K)

for 12 h that resulted in nanoperovskites with a homogeneous size distribution around 40 nm.

Powder XRD data were collected on a PANalytical X'Pert PRO diffractometer (Bragg–Brentano geometry) with an X'Celerator detector using the  $\text{Cu K}\alpha_1$  radiation ( $\lambda = 1.5405 \text{ \AA}$ ) in the angular range  $5^\circ < 2\theta < 80^\circ$ , by continuous scanning with a step size of  $0.02^\circ$ . For HP-XRD experiments, we have used a Rigaku SuperNOVA diffractometer equipped with an EOS detector and Mo radiation microsource ( $\lambda = 0.71073 \text{ \AA}$ ). A Diacell Bragg-S Diamond anvil cell from Almax-Easylab, with an opening angle close to  $90^\circ$  and anvil culets of 600  $\mu\text{m}$ , fitted with a stainless gasket containing a hole of 200  $\mu\text{m}$  diameter and 60  $\mu\text{m}$  depth was employed. A methanol–ethanol–water mixture (16:3:1) was used as a pressure-transmitting medium, which remains hydrostatic in the range of pressure used for this experiment.

RS measurements on  $\text{YAlO}_3$  nanoperovskite powders at room temperature were performed in backscattering geometry, exciting with a laser source at 532 nm with an incident power of 50 mW and using a HORIBA Jobin Yvon LabRAM HR UV spectrometer in combination with a thermoelectrically cooled multichannel Synapse CCD detector with a resolution of  $2 \text{ cm}^{-1}$ . The beam was focused on the sample using a 50 $\times$  objective with a beam diameter of approximately 2  $\mu\text{m}$  at the sample. For HP-RS measurements up to 30 GPa, the sample was placed in a membrane-type DAC and a mixture of methanol–ethanol–water (16:3:1) was used as a pressure-transmitting medium. In spite of using a methanol–ethanol–water mixture above 10 GPa, where it behaves in a nonhydrostatic way, the influence of deviatoric stresses can be apparently neglected.<sup>44</sup> The pressure was estimated using the ruby fluorescence technique<sup>45</sup> with the pressure scale recalibrated by Syassen.<sup>46</sup> Experimental frequencies of the Raman modes were obtained by fitting peaks with a Voigt profile (Lorentzian convoluted with a Gaussian) after proper calibration and background subtraction of the experimental spectra. The Gaussian line width was fixed to the experimental setup resolution ( $2 \text{ cm}^{-1}$ ) in order to get the three variables of the Lorentzian profile for each peak.

## 3. AB INITIO SIMULATION DETAILS

Structural, vibrational, and elastic properties of bulk  $\text{YAlO}_3$  perovskite at HP were theoretically obtained by means of *ab initio* total energy calculations. The study was carried out in the framework of density functional theory (DFT).<sup>47</sup> This method allows an accurate description of the physical properties of semiconductors at HP.<sup>48</sup> The simulations were conducted with the Vienna *Ab Initio* Simulation Package (VASP)<sup>49</sup> using the projector-augmented wave scheme (PAW)<sup>50</sup> to take into account the full nodal character of the all-electron charge density in the core region. In the simulation, 11 valence electrons ( $4s^2 4p^6 5s^2 4d^1$ ) were used for yttrium, 3 valence electrons were considered for aluminum ( $3s^2 3p^1$ ), and 6 valence electrons for oxygen ( $2s^2 2p^4$ ). The presence of oxygen in  $\text{YAlO}_3$  makes necessary the development of the set of plane waves up to a high energy cutoff of 520 eV. The exchange–correlation energy was described employing the generalized-gradient approximation (GGA) with the Perdew–Burke–Ernzenhof prescription for solids (PBEsol).<sup>51</sup> Integrations within the Brillouin zone (BZ) were performed with a dense mesh ( $6 \times 4 \times 6$ ) of Monkhorst–Pack *k*-special points.<sup>52</sup> In this way, a high convergence of 1 meV per formula unit was accomplished. At a set of selected volumes, the lattice

parameters and atomic positions were fully optimized by calculating the forces on the atoms and the stress tensor. In the optimized resulting perovskite structures, the forces on the atoms were lower than 0.002 eV/Å and the deviation of the stress tensor components from the diagonal hydrostatic form less than 0.1 GPa. All of the calculations were performed at  $T = 0$  K; temperature effects are not included in our study.

The elastic properties and mechanical stability of  $\text{YAlO}_3$  were studied after computing the elastic constants that describe the mechanical properties of a material in the region of small deformations. These elastic constants were evaluated by computing the macroscopic stress for a small strain using the stress theorem.<sup>53</sup> According to their symmetry, the ground state and the fully optimized structures were strained in different directions.<sup>54</sup> The variation of the total energy was determined with a Taylor expansion of the total energy with respect to the employed strain.<sup>55</sup> The strain used in the calculations guarantees the harmonic behavior.

Lattice-dynamic calculations were carried out at the center of the Brillouin zone center ( $\Gamma$  point). The direct force-constant approach (or supercell method)<sup>56</sup> was employed, requiring highly converged results on forces. The diagonalization of the dynamical matrix determines the frequencies of Raman- and infrared-active modes as well as silent modes. From the calculations, the symmetries of the eigenvectors of the different vibrational modes are also identified at the  $\Gamma$  point.

The combination of experiments and DFT calculations is a powerful resource that leads to reliable results on the HP behavior of solids.<sup>57–60</sup> In addition to this, the combination of *ab initio* simulations with experimental studies also provides depth insight into the pressure behavior on the polyhedral compressibility, which is related to the macroscopic compression.<sup>61</sup>

## 4. RESULTS AND DISCUSSION

**4.1. Structure under Pressure.** Perovskites have the general formula  $\text{ABO}_3$  and present four formula units per unit cell. The structure is formed by corner-linked octahedral  $\text{BO}_6$  units, whereas A cations are located in the interstices of the structure, thus leading to dodecahedral  $\text{AO}_{12}$  units<sup>62</sup> (see Figure 1). Due to its high flexibility, the perovskite structure can crystallize in a huge number of space groups depending on the ratio of the cation sizes, which is responsible for tilts and twists of the octahedral units. In particular,  $\text{YAlO}_3$  crystallizes in the orthorhombic *Pnma* structure, a.k.a. *Pbnm* when a different setting is used.<sup>62</sup>

The XRD pattern of  $\text{YAlO}_3$  nanoparticles is shown in Figure 1, and it has been well indexed to a *Pnma* orthorhombic structure. This means that XRD measurements have confirmed that  $\text{YAlO}_3$  nanoparticles have the same perovskite-type structure as the bulk material. No amorphous phase was detected in the sample. The average grain size  $D$  has been determined from the Scherrer formula<sup>63</sup>

$$D = \frac{0.89\lambda}{\beta \cos \theta} \quad (1)$$

where  $\lambda = 1.5406$  Å,  $\beta$  is the full width at half-maximum of the peaks, and  $\theta$  is the angle of diffraction. An average grain size value of around 40 nm has been found. Crystal structure parameters have been calculated after fitting the profiles of the nanoperoovskites by the Rietveld method using the FULLPROF program (see Table 1). The reliability factors ( $\chi^2$ ,  $R_p$ ,  $R_{\text{exp}}$  and

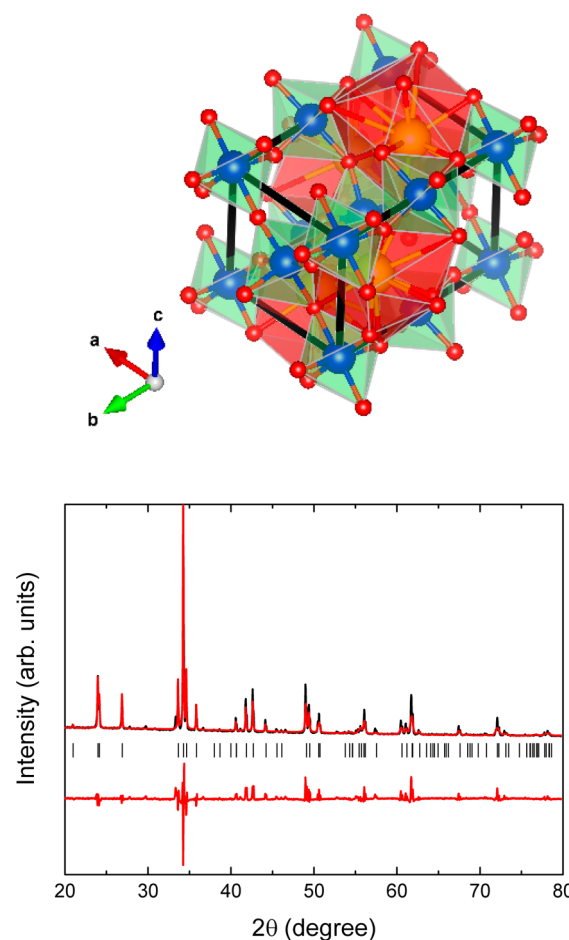


**Figure 1.** (a) Unit cell of the *Pnma*  $\text{YAlO}_3$  perovskite structure.  $\text{YO}_{12}$  dodecahedra (red) and  $\text{AlO}_6$  octahedra (green) are highlighted. Yellow spheres represent the Y atoms, blue ones correspond to the Al atoms, and the small red spheres to the O atoms. (b) XRD pattern of the  $\text{YAlO}_3$  nanoperoovskite. Rietveld refinements including the difference between calculated and observed patterns are also shown (red). The intensity of the peak at  $34.25^\circ$  has been divided by a factor of 4.

$R_{\text{Bragg}}$ ) obtained from this fitting were 4, 8.06, 16.8, and 0.02, respectively.

We have compared in Table 1 our *ab initio* calculated values of structural parameters of  $\text{YAlO}_3$  under ambient conditions with previous calculations and experimental values. As observed, there is a nice agreement between our theoretical data and experimental values. These results give us confidence in the goodness of our calculations. Furthermore, we have found that the experimental lattice parameters and atomic positions of  $\text{YAlO}_3$  nanoperoovskite with 40 nm in size are similar to those of bulk  $\text{YAlO}_3$ , clearly indicating that the structural properties of the bulk perovskite are reproduced in the nanoscale.

The structural properties of  $\text{YAlO}_3$  nanoperoovskite have been experimentally studied at different pressures up to 7 GPa. The values of the lattice parameters and the volume of the unit cell have been obtained from the profile matching of the XRD data and are shown in Figure 2. Since XRD measurements have been performed with a conventional diffractometer and with a small quantity of sample in the DAC, XRD patterns exhibit low intensity and do not have good statistics; thus, only profile matching of the XRD patterns was carried out. However, if our

**Table 1.** Structural Parameters and Atomic Positions of  $\text{YAlO}_3$  according to Setting 1 ( $Pnma$ ) under Ambient Conditions, Volume ( $V_0$ ), Bulk Modulus ( $B_0$ ), and Its First Derivative ( $B_0'$ )

	<i>ab initio</i> (this work)	<i>ab initio</i> <sup>a,b</sup>	<i>ab initio</i> <sup>a,c</sup> LDA	<i>ab initio</i> <sup>a,c</sup> GGA	experimental nano (this work)	experimental <sup>a,d</sup> bulk
<i>a</i> (Å)	5.332	5.27	5.27	5.41	5.327(2)	5.329
<i>b</i> (Å)	7.379	7.29	7.29	7.54	7.369(3)	7.370
<i>c</i> (Å)	5.177	5.13	5.12	5.31	5.175(3)	5.178
$V_0$ (Å <sup>3</sup> )	203.76	197.08	196.70	216.60	202.40(23)	203.44
Y (4c)	0.55, 0.25, 0.51	0.55, 0.25, 0.51			0.552(1), 0.25, 0.521(1)	0.55, 0.25, 0.51
Al (4b)	0, 0, 0.5	0, 0, 0.5			0, 0, 0.5	0, 0, 0.5
O (8d)	0.29, 0.04, 0.71	0.29, 0.04, 0.71			0.297(1), 0.004(1), 0.739(1)	0.29, 0.04, 0.70
O (4c)	0.98, 0.25, 0.41	0.98, 0.25, 0.42			0.973(1), 0.25, 0.448(1)	0.98, 0.25, 0.42
$B_0$ (GPa)	204.5		210.2	210.8	166(3)	192
$B_0'$	3.99		4.56	4.85	4	7.3

<sup>a</sup>Transformed into setting 1 ( $Pnma$ ) for better comparison with our results. <sup>b</sup>Reference 64. <sup>c</sup>Reference 40. <sup>d</sup>Reference 25. Our *ab initio* structural data are compared to other calculated data (refs 40 and 64) and experimental data for bulk (from ref 25) and nanocrystalline (our sample) perovskites.

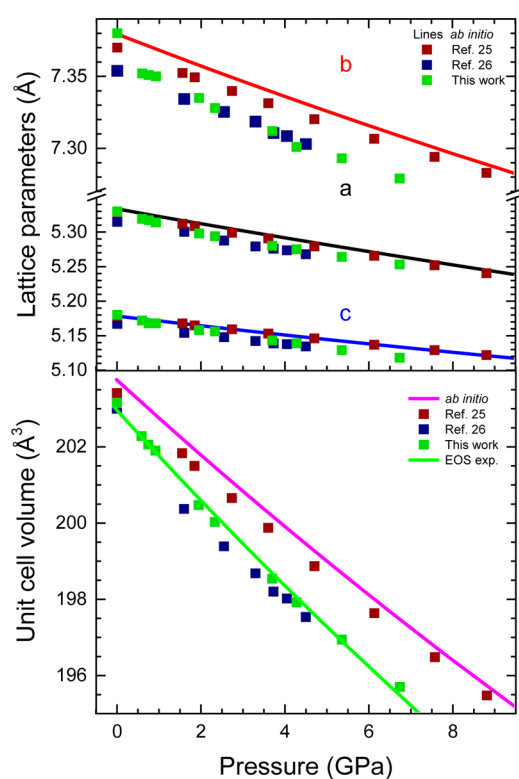


**Figure 2.** (a) Evolution with pressure of the lattice parameters and (b) the unit cell. Lattice parameters of refs 25 and 26 have been transformed into setting 1 ( $Pnma$ ) for better comparison with our results. Error bars are not shown in these figures because they are smaller than data symbols.

results are compared with those given by Ross et al.<sup>25,26</sup> (see Figure 2), who analyzed the XRD of  $\text{YAlO}_3$  single crystals as a function of pressure up to 9 GPa, it can be concluded that our study yields quite similar results to those of Ross et al. In fact, our lattice parameters and unit cell volume are slightly smaller than those presented in ref 25 and quite close to those of ref 26. Notice that data given by Ross et al. have been transformed into setting 1 ( $Pnma$ ) to get better comparison with our results.

In order to illustrate the structural changes of  $\text{YAlO}_3$  under pressure up to 95 GPa, we have performed *ab initio* calculations. Lattice parameters and the unit cell volume as well as the volumes of the dodecahedral ( $\text{YO}_{12}$ ) and octahedral ( $\text{AlO}_6$ ) units and the interatomic distances are shown in

Figures 2, 3, and 4. First of all, the evolution of the lattice parameters as a function of pressure is shown in Figures 2 and

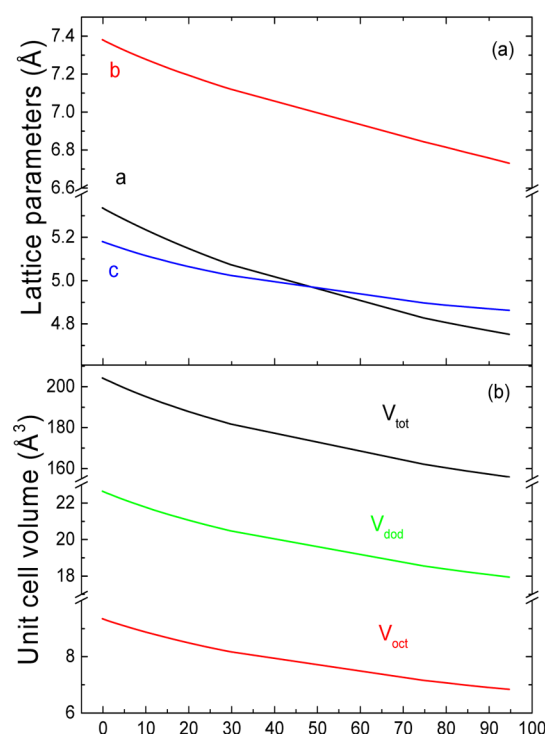


**Figure 3.** Theoretical pressure evolution of (a) the lattice parameters and (b) the unit cell, dodecahedral, and octahedral volumes of bulk  $\text{YAlO}_3$  up to 95 GPa.

3. It can be observed that *a*, *b*, and *c* lattice parameters decrease with pressure at different rates that agree with those obtained from XRD measurements. Taking into account the definition of the relative compressibility,  $\kappa$ , of a certain physical magnitude

$$\kappa_x = -\frac{1}{x_0} \frac{\partial x}{\partial P} \quad (2)$$

where  $x_0$  is the value of the magnitude at zero pressure, the calculated compressibilities of the *a*, *b*, and *c* lattice parameters are 2.02, 1.54, and 1.41 ( $\times 10^{-3} \text{ GPa}^{-1}$ ), respectively, with the *a*-axis being more compressible than the *b*- and *c*-axes. These values are in good agreement with those already reported for  $\text{YAlO}_3$  described with the  $Pbnm$  structure<sup>25</sup> where the *b*-axis,



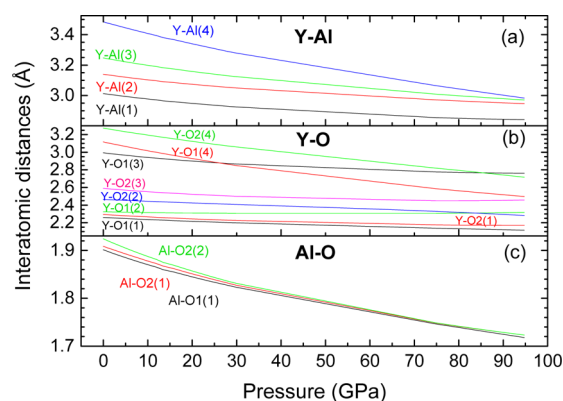


**Figure 4.** Pressure dependence of the theoretical interatomic distances in bulk  $\text{YAlO}_3$ : (a) Y–Al distances; (b) Y–O distances; (c) Al–O distances.

which corresponds to the  $a$ -axis in our setting, is also more compressible than the others, although slightly larger than those experimentally measured for single-crystalline and nanocrystalline  $\text{YAlO}_3$  perovskites (see Figure 2).

The pressure dependence of the unit cell volume of  $\text{YAlO}_3$  nanoperovskite is plotted in Figure 2, together with experimental data of refs 25 and 26 and *ab initio* calculation results. The pressure dependence of the unit cell volume of nanoperovskite  $\text{YAlO}_3$  fits better with data from ref 26. Our theoretical bulk modulus ( $B_0$ ), whose value is 204.5 GPa, is in agreement with the theoretical ones obtained by Huang et al.<sup>40</sup> (see Table 1). Our experimental unit cell volume as a function of pressure is well fitted to a second-order Birch–Murnaghan (BM2) equation of state (EOS),<sup>65</sup> yielding  $B_0 = 166.4$  GPa ( $B_0'$  fixed to 4).

The experimental  $B_0$  value in  $\text{YAlO}_3$  nanocrystals is  $\sim 14\%$  lower than the experimental value for bulk  $\text{YAlO}_3$  (192 GPa), as obtained by Ross et al.<sup>25</sup> by using a third-order Birch–Murnaghan (BM3) EOS (see Table 1). The fit of our data to a BM3 EOS yields  $B_0 = 133$  GPa with  $B_0' = 18$  (see the Supporting Information, section S3), which differs notably from the one obtained by Ross et al. ( $B_0 = 192$  GPa) and gives an unreliable  $B_0'$ .<sup>25</sup>

The pressure dependence of the  $\text{YO}_{12}$  dodecahedron ( $V_{\text{dod}}$ ),  $\text{AlO}_6$  octahedron ( $V_{\text{oct}}$ ), and unit cell volume ( $V_{\text{tot}}$ ) are plotted in Figure 3. Overall, all of these volumes decrease with pressure, with the octahedron volume showing a higher compressibility ( $5.6 \times 10^{-3} \text{ GPa}^{-1}$ ) than the dodecahedron one ( $4.35 \times 10^{-3} \text{ GPa}^{-1}$ ). These results are in good agreement with those of Ross et al.<sup>25,26</sup> Zhao et al.<sup>35</sup> reported that the ratio between  $\text{AO}_{12}$  dodecahedron and  $\text{BO}_6$  octahedron compressibilities ( $\kappa_{\text{dod}}/\kappa_{\text{oct}}$ ) allows one to know the distortion degree of the structure with pressure toward more distorted or more symmetrical structures. When  $\kappa_{\text{dod}}/\kappa_{\text{oct}} > 1$ ,  $\text{BO}_6$  octahedra are more distorted with pressure compared with  $\text{AO}_{12}$  dodecahedra, thus suggesting that the structure becomes less symmetrical with pressure. Conversely,  $\text{AO}_{12}$  dodecahedra are more distorted than  $\text{BO}_6$  octahedra on increasing pressure when  $\kappa_{\text{dod}}/\kappa_{\text{oct}} < 1$ , thus suggesting that the structure becomes more symmetrical with pressure and a tendency to undergo a phase transition to a cubic perovskite structure. Finally, both polyhedral units evolve in a similar way with pressure when  $\kappa_{\text{dod}}/\kappa_{\text{oct}} \cong 1$ , so in this case, pressure does not cause any distortion in the structure. According to our results,  $\text{AlO}_6$  octahedral units present a higher compressibility than  $\text{YO}_{12}$  dodecahedral units. In particular,

$\kappa_{\text{dod}}/\kappa_{\text{oct}} \cong 0.78$  at ambient pressure and it is always below 1 in the whole pressure range up to 95 GPa; therefore, our calculations indicate that  $\text{YAlO}_3$  evolves toward a more symmetrical structure with increasing pressure, in good agreement with data reported in the literature.<sup>25,26,29</sup> It is also relevant to mention that this evolution toward more symmetrical structures occurs in other perovskites too, for instance, in orthorhombic  $\text{GdAlO}_3$ ,  $\text{GdFeO}_3$ , and  $\text{ScAlO}_3$  perovskites,<sup>26,31,35</sup> suggesting that the evolution toward a more symmetrical structure seems to be a general behavior in orthorhombic perovskites. In this respect, we have evaluated the departure of the orthorhombic structure of  $\text{YAlO}_3$  from the cubic archetype one by calculating the cell distortion factor,  $d$ , introduced by Sasaki et al.<sup>66</sup> The normalized cell distortion factor with pressure,  $d_{\text{norm}}(P)$ , decreases as pressure increases in  $\text{YAlO}_3$  nanoperovskites in good agreement with bulk  $\text{YAlO}_3$  (see section S4 in the Supporting Information).<sup>67</sup>

The evolution of the interatomic distances with pressure up to 95 GPa is shown in Figure 4. Concerning the Y–O interatomic distances (see Table 2), it can be observed that

**Table 2.** Nearest-Neighbor Cation–Anion Distances in Bulk  $\text{YAlO}_3$  at Selected Pressures<sup>a</sup>

	cation–anion distances (Å)		
	0 GPa	30 GPa	75 GPa
Y–O1 (1)	2.25307(1)	2.19074(1)	2.13078(1)
Y–O1 (2)	2.31767(1)	2.2991(1)	2.29936(1)
Y–O1 (3)	2.98824(1)	2.8434(1)	2.57966(1)
Y–O1 (4)	3.11212(1)	2.86012(1)	2.77046(1)
Y–O2 (1)	2.28602(1) (x2)	2.21788(1) (x2)	2.1677(1) (x2)
Y–O2 (2)	2.45827(1) (x2)	2.40035(1) (x2)	2.3209(1) (x2)
Y–O2 (3)	2.58368(1) (x2)	2.49305(1) (x2)	2.44245(1) (x2)
Y–O2 (4)	3.26932(1) (x2)	3.05455(1) (x2)	2.81457(1) (x2)
Al–O1 (1)	1.89981(1) (x2)	1.82132(1) (x2)	1.74460(1) (x2)
Al–O2 (1)	1.90706(1) (x2)	1.82561(1) (x2)	1.74636(1) (x2)
Al–O2 (2)	1.92292(1) (x2)	1.82949(1) (x2)	1.74677(1) (x2)

<sup>a</sup>O1 and O2 refer to the oxygens in the 4c and 8d Wyckoff positions, respectively. Numbers (1), (2), (3), and (4) refer to different Y–O and Al–O distances in the dodecahedron ( $\text{YO}_{12}$ ) and octahedron ( $\text{AlO}_6$ ), respectively.

some of them have similar decreasing rates with pressure:  $-2.72$ ,  $-3.07$ , and  $-2.4 \times 10^{-3} \text{ Å} \cdot \text{GPa}^{-1}$  for Y–O1(1), Y–O2(1), and Y–O2(2), respectively. On the other hand, the Y–O2(3), Y–O1(3), and Y–O2(4) interatomic distances present decreasing rates of  $-4.41$ ,  $-5.94$ , and  $-8.33 \times 10^{-3} \text{ Å} \cdot \text{GPa}^{-1}$ . The Y–O1(4) distance shows the highest decreasing rate ( $-10.06 \times 10^{-3} \text{ Å} \cdot \text{GPa}^{-1}$ ), whereas Y–O1(2) shows the smallest one ( $-1.2 \times 10^{-3} \text{ Å} \cdot \text{GPa}^{-1}$ ). The Al–O interatomic distances decrease with pressure with similar rates (around  $-4.07 \times 10^{-3} \text{ Å} \cdot \text{GPa}^{-1}$ ), whereas all of the Y–Al interatomic distances decrease with pressure as well, with the Y–Al(4) with a decrease rate of  $-8.18 \times 10^{-3} \text{ Å} \cdot \text{GPa}^{-1}$  being more significant. The large compressibility of Y–O1(4), Y–O2(4), and Y–O1(3) distances shown in Figure 4 clearly indicates that the coordination of Y in  $\text{YAlO}_3$  at ambient pressure is indeed smaller than 12 (in fact, it is around  $8 + 4$ , since there are four distances above 3 Å at ambient pressure) and that it tends to  $9 + 3$  on increasing pressure.

**4.2. Raman Spectroscopy.** According to theoretical considerations, the  $Pnma$  structure of  $\text{YAlO}_3$  with four formula units per primitive cell has 60 vibrational modes distributed in

24 Raman-active modes ( $\Gamma_R$ ), 25 infrared-active modes ( $\Gamma_{IR}$ ), 8 optically inactive (silent) modes ( $\Gamma_S$ ), and 3 acoustic ( $\Gamma_{AC}$ ) modes:

$$\begin{aligned}\Gamma_R &= 7A_g + 5B_{1g} + 7B_{2g} + 5B_{3g} \\ \Gamma_{IR} &= 9B_{1u} + 7B_{2u} + 9B_{3u} \\ \Gamma_S &= 8A_u \\ \Gamma_{AC} &= B_{1u} + B_{2u} + B_{3u}\end{aligned}\quad (3)$$

In the following, we will analyze the lattice dynamics of  $YAlO_3$  at ambient as well as at high pressures. A superindex has been added to the vibrational modes in order of increasing frequency.

**4.2.1. Ambient Pressure.** The Raman scattering (RS) spectrum of  $YAlO_3$  nanoperovskite at ambient conditions is shown in Figure 5. Around 23 lines have been observed, but

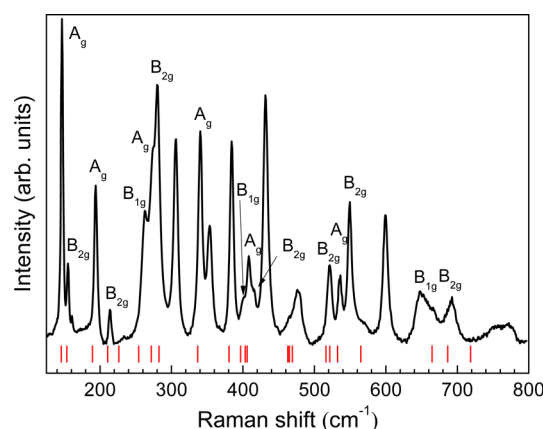


**Figure 5.** RS spectrum of  $YAlO_3$  nanoperovskite obtained ambient conditions. Vertical lines indicate the *ab initio* frequencies of first-order Raman-active modes.

not all of them correspond to first-order Raman-active modes. Only 16 out of 24 first-order Raman-active modes theoretically predicted have been observed, while the rest have been attributed to second-order vibrational modes. The absence of the rest of the Raman-active modes could be due to accidental degeneracy of several modes or due to their weakness. For comparison, vertical marks at the bottom of the figure, which represent the theoretical Raman-active mode frequencies predicted under ambient conditions for bulk  $YAlO_3$ , were also included in Figure 5. The symmetries of the observed modes are assigned with the help of our theoretical calculations (based on both Raman-active frequencies and pressure coefficients). Experimental and theoretical frequencies of the Raman-active modes for  $YAlO_3$  at ambient pressure are exposed in Table 3.

The comparison of the experimental RS spectrum of  $YAlO_3$  nanoperovskite with other RS spectra of perovskite crystals, but containing different elements other than Y in site A and Al in site B, found in the literature hints that changing elements that occupy crystal sites A or B should selectively affect different vibrational modes: changing the element in site A should mainly affect modes involving rare earth ions, such as Y or Gd, in  $AO_{12}$  units without significant variations on the vibrational modes related to  $BO_6$  octahedra. For instance, Chopelas et al.<sup>68</sup> compared the Raman frequencies of  $YAlO_3$  and  $GdAlO_3$  perovskites, and as expected, the low energy modes of

$GdAlO_3$  were lower than those in  $YAlO_3$  due to the larger mass of Gd compared to Y. This result was corroborated by Andreasson et al.<sup>69</sup>

Traditionally, changes in the RS spectrum of  $ABO_3$  perovskites, with A being a rare earth, are attributed either to the effects of the unit cell dimension or the A cation mass. In the region of low frequencies, the main effect is given by A cation mass that, considering the harmonic approximation, goes as the square root of its mass,  $m_A^{-1/2}$ , since the ratio of the strength of the chemical bonding and the cation mass is mainly dominated by the latter. In the region of high frequencies, the principal effect is the different size of the unit cell that mainly depends on the strength of the B–O bonds.<sup>68</sup>

Taking into account the above considerations and comparing with vibrational frequencies of other perovskites (Table 3), it is reasonable that the low-frequency Raman modes in  $YAlO_3$  nanoperovskite are practically the same (see the lowest frequency Raman  $A_g^1$  mode in Table 3) as in  $YCrO_3$ , whereas the high-frequency Raman modes of  $YAlO_3$  nanoperovskite are shifted to high energies compared to those of  $YCrO_3$ .<sup>70</sup> Similarly, it can be observed that the low-frequency Raman modes of  $YAlO_3$  nanoperovskite (for example, the lowest frequency Raman  $A_g^1$  mode in Table 3) are shifted to higher frequencies with respect to  $GdAlO_3$ , whereas the high-frequency Raman modes are similar for both compounds.<sup>68</sup> Finally, we want to mention that we have found that the experimental data of the Raman mode frequencies of  $YAlO_3$  nanoperovskite are similar to those found in the literature for  $YAlO_3$  bulk (see Table 3), thus suggesting that nano- $YAlO_3$  behaves as its bulk counterpart but in the nanoscale. This is in good agreement with the structural results discussed in the previous section.

It is worth noting that our measurements in  $YAlO_3$  nanoperovskite and the help of lattice dynamics calculations have allowed the nature of the high-frequency modes to be clarified. Raman modes with frequencies around 663 and 694  $cm^{-1}$  correspond to the theoretically proposed modes  $B_{1g}^5$  and  $B_{2g}^7$ , respectively. Such modes were not reported as the highest Raman mode frequencies in previous studies of bulk  $YAlO_3$ , but they were assumed to be those at 550 ( $A_g^7$ ), 552 ( $A_g^7$ ), and 555  $cm^{-1}$  ( $B_{1g}^4$ ), respectively.<sup>68,70,71</sup>

For comparison with other perovskites, it is better to divide the Raman spectrum of nano- $YAlO_3$  into two regions:<sup>72</sup> the low-frequency region up to  $\sim 280\text{ cm}^{-1}$ , which corresponds to the vibrations of Y–O (frequencies in this region are more or less unchanged with the B atom; see  $YAlO_3$  and  $YCrO_3$  in Table 3), and the high-frequency region from  $280\text{ cm}^{-1}$  onward, which is related to the vibrational modes of the oxygens and in terms of the molecular structure to the  $AlO_6$  octahedra. The symmetries of the observed modes are indexed on the basis of our theoretical calculations and on the comparison with previous studies of lattice dynamics in orthorhombic perovskites.<sup>70,72–74</sup> The nonindexed peaks likely correspond to second-order Raman modes. Overall, there is a good agreement between the experimental results in  $YAlO_3$  nanoperovskite and the theoretical ones at ambient conditions (see Table 3). Note that there are some differences between the experimental and theoretical Raman-mode frequencies, which can be attributed to the GGA approximation that tends to underestimate vibrational frequencies.

The RS spectrum of perovskites can be interpreted assuming that the different Raman modes could be associated with the vibrational modes of dodecahedron ( $YO_{12}$ ) and octahedral

Table 3. Theoretical and Experimental Raman Frequencies of Several Orthorhombic ABO<sub>3</sub> Perovskites<sup>a</sup>

mode	YAlO <sub>3</sub> , this work			YAlO <sub>3</sub> , ref 64	YAlO <sub>3</sub> , ref 71	YAlO <sub>3</sub> , ref 68	YAlO <sub>3</sub> , ref 70	YCrO <sub>3</sub> , ref 70	GdAlO <sub>3</sub> , ref 68
	theo. (cm <sup>-1</sup> )	Exp. (cm <sup>-1</sup> )	AlO <sub>6</sub> motion	theo. (cm <sup>-1</sup> )	exp. (cm <sup>-1</sup> )	exp. (cm <sup>-1</sup> )	exp. (cm <sup>-1</sup> )	exp. (cm <sup>-1</sup> )	exp. (cm <sup>-1</sup> )
A <sub>g</sub> <sup>1</sup>	146(2)	147(2)		147.3	152	148	150	156	95
B <sub>2g</sub> <sup>1</sup>	154(2)	156(2)		157.9		157	157		111
B <sub>3g</sub> <sup>1</sup>	189(2)			198	152	194	197	176	146
A <sub>g</sub> <sup>2</sup>	189(2)	195(2)		196.4	197	195	197	188	146
B <sub>2g</sub> <sup>2</sup>	211(2)	215(2)		216.1		216	219	223	160
B <sub>1g</sub> <sup>1</sup>	226(2)		B <sub>1g</sub> (3)	233.8	160				174
B <sub>1g</sub> <sup>2</sup>	254(2)	264(2)		259.7	218	216	270	272	217
A <sub>g</sub> <sup>3</sup>	272(2)	274(2)		277.4	280	275	278	282	232
B <sub>2g</sub> <sup>3</sup>	282(2)	281(2)		283.6	267	284			222
A <sub>g</sub> <sup>4</sup>	337(2)	341(2)	A <sub>g</sub> (2)	342.1	350	343	345	346	313
B <sub>3g</sub> <sup>2</sup>	381(2)		B <sub>3g</sub> (4)	394.4					
B <sub>1g</sub> <sup>3</sup>	397(2)	403(2)	B <sub>1g</sub> (4)	406.4	287	265	403	413	323
A <sub>g</sub> <sup>5</sup>	403(2)	416(2)	A <sub>g</sub> (1)	409	415	411	412	429	368
B <sub>2g</sub> <sup>4</sup>	406(2)	409(2)	B <sub>2g</sub> (4)	418	407		283	318	
B <sub>1g</sub> <sup>4</sup>	463(2)		B <sub>1g</sub> (2)	464.2	422	403	555		400
A <sub>g</sub> <sup>6</sup>	465(2)		A <sub>g</sub> (3)	469.2		438		492	
B <sub>3g</sub> <sup>3</sup>	469(2)		B <sub>3g</sub> (2)	470.8			470	487	398
B <sub>3g</sub> <sup>4</sup>	516(2)		B <sub>3g</sub> (3)	531			540	569	475
B <sub>2g</sub> <sup>5</sup>	521(2)	523(2)	B <sub>2g</sub> (3)	536.1		418		502	414
A <sub>g</sub> <sup>7</sup>	532(2)	537(2)	A <sub>g</sub> (4)	547.4	550	552	553	566	536
B <sub>2g</sub> <sup>6</sup>	564(2)	551(2)	B <sub>2g</sub> (2)	581.3		543	552		512
B <sub>1g</sub> <sup>5</sup>	664(2)	663(2)	B <sub>1g</sub> (1)	675.9					551
B <sub>2g</sub> <sup>7</sup>	686(2)	694(2)	B <sub>2g</sub> (1)	697.7					
B <sub>3g</sub> <sup>5</sup>	718(2)		B <sub>3g</sub> (1)	731.5	545	527			523

<sup>a</sup>Our values are compared to other theoretical and experimental values of Raman frequencies for bulk YAlO<sub>3</sub> and also to others ABO<sub>3</sub> compounds with *Pnma* structure. The AlO<sub>6</sub> motion assignment is also given according to ref 73.

(AlO<sub>6</sub>) units. Nevertheless, this assignment is not straightforward, since these vibrational modes are coupled to each other. Therefore, and in order to understand the contribution of each polyhedral unit to every Raman mode, a calculation of the phonon density of states is required (see Figure 6). According to these results, Y atoms with dodecahedral coordination (YO<sub>12</sub>) mainly contribute in the low-frequency region up to ~300 cm<sup>-1</sup>, showing a maximum centered around 150 cm<sup>-1</sup>. A minor contribution of this unit can be observed in the region between 300 and 500 cm<sup>-1</sup>. On the other hand, Al atoms with octahedral coordination (AlO<sub>6</sub>) present a high contribution in

the region between ~300 and 750 cm<sup>-1</sup>. The major contribution of this unit is around 420 cm<sup>-1</sup>. It is relevant to notice that Al and O atoms contribute in both the low- and high-frequency regions, and that there is a small region between 220 and 300 cm<sup>-1</sup> where Y and Al atoms have similar contributions.

Once the contributions of the individual atoms are known, it is possible to discuss the contributions of the polyhedra to each vibrational mode. The phonon modes of a perovskite with the general formula ABO<sub>3</sub> can be described as a combination of the molecular modes of the BO<sub>6</sub> units. This feature was used to describe the phonon modes of other similar perovskites.<sup>72,73</sup>

Concerning the contribution of the polyhedral units to each vibrational mode, the A<sub>g</sub><sup>1</sup> (146 cm<sup>-1</sup>), B<sub>2g</sub><sup>1</sup> (154 cm<sup>-1</sup>), B<sub>3g</sub><sup>1</sup> (189 cm<sup>-1</sup>), A<sub>g</sub><sup>2</sup> (189 cm<sup>-1</sup>), and B<sub>2g</sub><sup>2</sup> (210 cm<sup>-1</sup>) modes of the low-frequency region are all associated with translational motions of the YO<sub>12</sub> units without any contribution of AlO<sub>6</sub> units. The B<sub>1g</sub><sup>2</sup> (254 cm<sup>-1</sup>), A<sub>g</sub><sup>3</sup> (271 cm<sup>-1</sup>), and B<sub>2g</sub><sup>3</sup> (282 cm<sup>-1</sup>) modes correspond to rotational movements of YO<sub>12</sub> dodecahedra where there is an almost equal contribution of AlO<sub>6</sub> units. Regarding the high-frequency region, which is mainly due to AlO<sub>6</sub> octahedral motions (see Table 3), the A<sub>g</sub><sup>4</sup> (336 cm<sup>-1</sup>), B<sub>3g</sub><sup>2</sup> (380 cm<sup>-1</sup>), B<sub>2g</sub><sup>4</sup> (406 cm<sup>-1</sup>), and A<sub>g</sub><sup>7</sup> (532 cm<sup>-1</sup>) modes are related to rotations of AlO<sub>6</sub> units. On the other hand, the A<sub>g</sub><sup>6</sup> (465 cm<sup>-1</sup>), B<sub>3g</sub><sup>4</sup> (516 cm<sup>-1</sup>), B<sub>2g</sub><sup>5</sup> (521 cm<sup>-1</sup>), and B<sub>2g</sub><sup>6</sup> (564 cm<sup>-1</sup>) modes are mainly related to bending motions of AlO<sub>6</sub> units. Finally, the A<sub>g</sub><sup>5</sup> (403 cm<sup>-1</sup>), B<sub>1g</sub><sup>4</sup> (463 cm<sup>-1</sup>), B<sub>3g</sub><sup>3</sup> (469 cm<sup>-1</sup>), B<sub>1g</sub><sup>5</sup> (664 cm<sup>-1</sup>), B<sub>2g</sub><sup>7</sup> (686 cm<sup>-1</sup>), and B<sub>3g</sub><sup>5</sup> (718 cm<sup>-1</sup>) modes mainly correspond to stretching movements of AlO<sub>6</sub> units.

**4.2.2. High Pressure.** Selected RS spectra of YAlO<sub>3</sub> nanoperovskite at different pressures up to 30 GPa are depicted

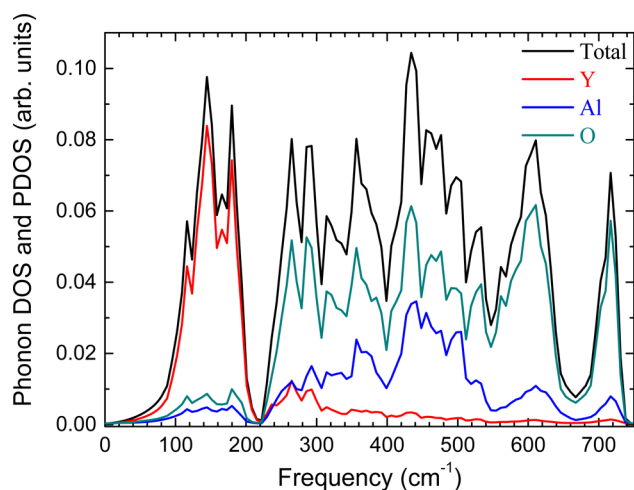
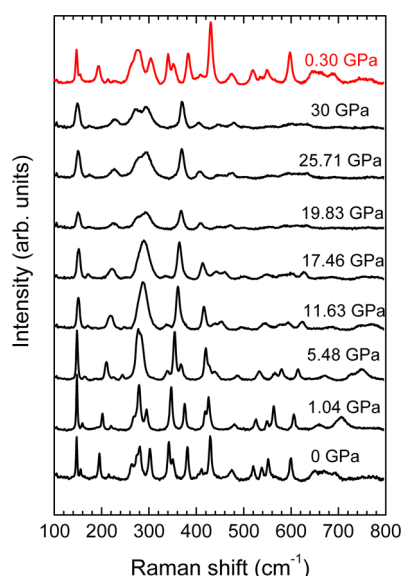


Figure 6. Partial and total phonon density of states of YAlO<sub>3</sub>. The total phonon density is represented by the black curve.



in Figure 7. Although only 16 out of 24 Raman-active first-order modes were observed at ambient pressure, the number of



**Figure 7.** Selected experimental RS spectra of YAlO<sub>3</sub> nanoperovskite at different pressures up to 30 GPa. The Raman scattering spectrum at the top (red curve) is taken at 0.3 GPa after releasing pressure.

the observed Raman peaks changes as the pressure increases. In fact, the intensity of some peaks decreases with increasing pressure while others simply disappear. As a general rule, all phonon frequencies show a monotonous increase with pressure up to 30 GPa, except the B<sub>2g</sub><sup>3</sup> mode near 280 cm<sup>−1</sup> which exhibits a slight shift to lower frequencies. At 4.36 GPa, we observed the appearance of the B<sub>1g</sub><sup>1</sup> mode near 239.5 cm<sup>−1</sup>. Appreciable broadening was observed in the Raman peaks from ~10 GPa due to the partial loss of the hydrostatic conditions of the pressure-transmitting medium. However, the profiles of the Raman modes in the RS spectra do not change up to 30 GPa, so it can be concluded that the sample is stable in the *Pnma* phase up to this pressure. Furthermore, the RS spectrum obtained at 0.30 GPa after releasing pressure (see the RS spectrum at the top of Figure 7) is similar to the one obtained at ambient pressure before applying pressure (RS spectrum at the bottom of Figure 7), thus indicating a reversibility of the changes induced by pressure.

The pressure dependence of the experimental and theoretical Raman-active mode frequencies up to 30 GPa is depicted in Figure 8.

It can be observed that first-order pressure coefficients at ambient pressure are positive except for the B<sub>2g</sub><sup>3</sup> mode at 282 cm<sup>−1</sup> (−0.23 cm<sup>−1</sup> GPa<sup>−1</sup>). In addition, the lowest-frequency Raman phonon mode A<sub>g</sub><sup>1</sup> has a very small pressure coefficient (0.11 cm<sup>−1</sup> GPa<sup>−1</sup>), which means that this mode shows a negligible dependence with volume and only depends on the mass of the A cation, as already commented. Table 4 summarizes the theoretical and experimental frequencies and pressure coefficients of the different Raman-active modes in YAlO<sub>3</sub> after fit to equation

$$\omega = \omega_0 \left( \frac{\partial \omega}{\partial P} \right) P + \frac{1}{2} \left( \frac{\partial^2 \omega}{\partial P^2} \right) P^2 \quad (4)$$

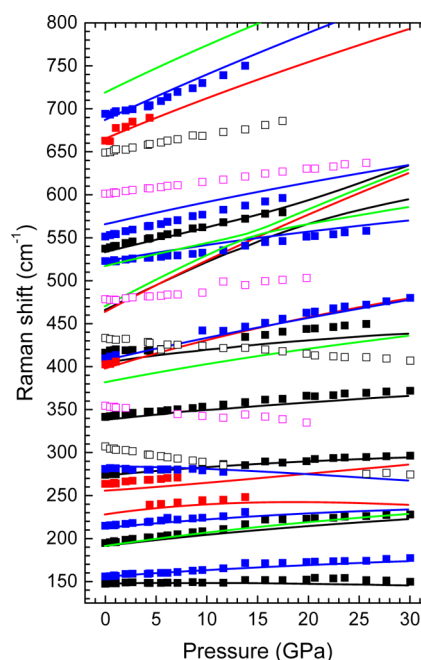


**Figure 8.** Pressure dependence of all peaks observed in RS spectra of YAlO<sub>3</sub> nanoperovskite (symbols) compared to theoretical data for bulk YAlO<sub>3</sub> (lines). Raman-active modes with different symmetry show different colors: A<sub>g</sub> (black), B<sub>1g</sub> (red), B<sub>2g</sub> (blue), and B<sub>3g</sub> (green). Open symbols correspond to other modes which likely correspond to second-order Raman modes despite the presence of photoluminescence lines cannot be fully discarded. Error bars are not included in this figure because they are shorter than data symbols.

The experimental and theoretical Grüneisen parameters,  $\gamma = -(B_0/\omega_0)(\partial\omega/\partial P)$ , for the Raman modes are also given in Table 4. The former parameters have been calculated by employing the theoretical bulk modulus,  $B_0 = 204.5$  GPa, estimated from the third-order Birch–Murnaghan EOS.<sup>75</sup> It can be observed that theoretical and experimental Grüneisen parameters show a notable variation in both low- and high-frequency regions, with the last one being more noticeable, indicating that the restoring forces on the atoms of AlO<sub>6</sub> polyhedra are larger than YO<sub>12</sub> ones. The A<sub>g</sub><sup>1</sup> mode, the lowest in frequency, corresponds to the translational motion of the YO<sub>12</sub> unit and shows a very small pressure coefficient and Grüneisen parameter at ambient pressure.

Four peaks observed in the RS spectrum, around 355, 479, 601, and 649 cm<sup>−1</sup>, do not correspond to first-order Raman active modes, as can be observed by comparison with our theoretical calculations. These modes are likely related to second-order Raman modes and not to photoluminescence lines, because chemical analysis corroborates the purity of our sample and the lack of doping with optically active ions. In any case, the presence of photoluminescence lines cannot be fully discarded, since these lines could appear for ions with a concentration below our detection limit. It is relevant to notice that the larger contraction of distances related to yttrium (Y–O) is reflected in the larger pressure coefficients for the modes related to Y atoms, between 146 and ~280 cm<sup>−1</sup>, than those corresponding to AlO<sub>6</sub> units, which are usually located in the high-frequency region.

The presence of negative slopes with pressure in Raman modes, such as the B<sub>2g</sub><sup>3</sup> Raman mode at 282 cm<sup>−1</sup>, indicates the softening of several bonds with increasing pressure. Nonetheless, the negative pressure coefficients of these modes cannot be



**Table 4.** Theoretical (Bulk) and Experimental (Nano-Perovskite) First-Order Raman-Active Mode Frequencies, Pressure Coefficients, and Grüneisen Parameters in YAlO<sub>3</sub> up to 30 GPa<sup>a</sup>

mode	theory				experiment			
	$\omega_0$ (cm <sup>-1</sup> )	$\partial\omega/\partial P$ (cm <sup>-1</sup> GPa <sup>-1</sup> )	$\partial^2\omega/\partial P^2$ (cm <sup>-1</sup> GPa <sup>-2</sup> × 10 <sup>3</sup> )	$\gamma$	$\omega_0$ (cm <sup>-1</sup> )	$\partial\omega/\partial P$ (cm <sup>-1</sup> GPa <sup>-1</sup> )	$\partial^2\omega/\partial P^2$ (cm <sup>-1</sup> GPa <sup>-2</sup> × 10 <sup>3</sup> )	$\gamma$
A <sub>g</sub> <sup>1</sup>	146(2)	0.11(2)	-13(2)	0.15	147(2)	0.40(2)	-16(2)	0.56
B <sub>2g</sub> <sup>1</sup>	154(2)	0.81(2)	-14(3)	1.08	156(2)	1.09(1)	-24(3)	1.45
B <sub>3g</sub> <sup>1</sup>	189(2)	1.67(1)	-20(1)	1.81			0	
A <sub>g</sub> <sup>2</sup>	189(2)	1.40(2)	-24(2)	1.51	195(2)	1.96(2)	-54(2)	2.12
B <sub>2g</sub> <sup>2</sup>	211(2)	1.09(2)	-26(1)	1.06	215(2)	1.04(3)	3.0(1)	1.01
B <sub>1g</sub> <sup>1</sup>	226(2)	1.47(2)	-80(3)	1.33		0.77(1)	132(1)	
B <sub>1g</sub> <sup>2</sup>	254(2)	0.90(2)	8.0(1)	0.72	264(2) <sup>b</sup>	1.43(2) <sup>b</sup>	-106(2) <sup>b</sup>	1.15
A <sub>g</sub> <sup>3</sup>	272(2)	1.08(3)	-26(2)	0.81	274(2)	0.99(4)	-20(3)	0.74
B <sub>2g</sub> <sup>3</sup>	282(2)	-0.23(1)	-23(3)	-0.17	281(2)	-0.1(1)	-28(3)	-0.07
A <sub>g</sub> <sup>4</sup>	337(2)	1.21(3)	-19(1)	0.73	341(2)	1.42(2)	-26(2)	0.86
B <sub>3g</sub> <sup>2</sup>	380(2)	2.23(3)	-29(2)	1.20				
B <sub>1g</sub> <sup>3</sup>	397(2)	3.51(1)	-54(1)	1.81	403(2)	3.24(2)	-62(2)	1.64
A <sub>g</sub> <sup>5</sup>	403(2)	1.65(2)	-36(1)	0.84	416(2)	1.10(3)	20(2)	0.54
B <sub>2g</sub> <sup>4</sup>	406(2)	2.72(2)	-24(1)	1.37	409(2)	3.15(2)	-54(3)	1.57
B <sub>1g</sub> <sup>4</sup>	463(2)	6.06(2)	-46(3)					
A <sub>g</sub> <sup>6</sup>	465(2)	6.44(2)	-140(2)	2.83				
B <sub>3g</sub> <sup>3</sup>	469(2)	7.04(1)	-216(2)	3.07				
B <sub>3g</sub> <sup>4</sup>	516(2)	1.93(1)	-123(2)	0.76				
B <sub>2g</sub> <sup>5</sup>	521(2)	2.03(1)	-30(2)	0.80	523(2)	1.12(2)	28(2)	0.44
A <sub>g</sub> <sup>7</sup>	532(2)	2.38(2)	-62(2)	0.91	537(2)	2.76(2)	-36(3)	1.06
B <sub>2g</sub> <sup>6</sup>	565(2)	2.69(4)	-27(2)	0.97	551(2)	2.79(3)	-26(2)	1.10
B <sub>1g</sub> <sup>5</sup>	665(2)	4.86(3)	29(1)	1.49	663(2) <sup>b</sup>	12.54(2) <sup>b</sup>	-3 × 10 <sup>3</sup> <sup>b</sup>	3.86
B <sub>2g</sub> <sup>7</sup>	686(2)	5.42(3)	-37(3)	1.62	694(2)	4.50(4)	28(1)	1.34
B <sub>3g</sub> <sup>5</sup>	719(2)	5.65(2)	-46(3)	1.61				

<sup>a</sup>The second-order polynomial fit was used in order to obtain the pressure dependence of both theoretical and experimental frequencies. <sup>b</sup>The slope of this experimental value differs significantly from the theoretical value likely because of the lack of experimental data in a wider pressure range.

directly related to structural instabilities, because no phase transition was observed either in our experiments up to 30 GPa or in our calculations: no mechanical instability up to 92 GPa, as it will be discussed in the last section of this work; and no dynamical instability (zero frequency mode) up to 100 GPa. It is relevant to mention that we did not find any imaginary phonon at any pressure, neither in Raman, infrared, or silent modes up to 100 GPa. The smaller silent mode at 100 GPa is one A<sub>u</sub> mode with a frequency of 167.6 cm<sup>-1</sup>.

Additionally, Figure 9a shows the pressure dependence of the theoretical frequencies of infrared-active (IR) modes (B<sub>1u</sub>, B<sub>2u</sub>, and B<sub>3u</sub>) for bulk YAlO<sub>3</sub>. IR frequencies, pressure coefficients, and Grüneisen parameters after fits to eq 4 are given in Table 5. As observed, theoretical Grüneisen parameters of IR-active modes vary between 0.76 and 2.4 in a similar fashion as Raman-active modes. Finally, the pressure dependence of the frequencies of the silent (A<sub>u</sub>) vibrational modes, which are active in hyper-Raman scattering, are plotted in Figure 9b.

In summary, our lattice dynamics calculations are in good agreement with experimental measurements on YAlO<sub>3</sub> nano-perovskite, thus confirming the large similitude between the bulk properties and those found in the 40 nm size nanoparticles, as was also previously found in nanogarnets with similar sizes.<sup>76,77</sup> Furthermore, they show the dynamical stability of the perovskite *Pnma* structure in YAlO<sub>3</sub> at least up to 30 GPa, thus suggesting that the related compound GdAlO<sub>3</sub> should not undergo a phase transition above 12 GPa, as previously suggested by Ross et al. from extrapolation of low-pressure data.<sup>78</sup>

**4.3. Elastic Properties.** The study of the elastic constants of materials is useful in order to understand their mechanical and thermodynamical properties as well as their structural stability. Orthorhombic YAlO<sub>3</sub> crystals are characterized by an elastic constant tensor with nine independent elastic constants: C<sub>11</sub>, C<sub>22</sub>, C<sub>33</sub>, C<sub>44</sub>, C<sub>55</sub>, C<sub>66</sub>, C<sub>12</sub>, C<sub>13</sub>, and C<sub>23</sub>. The values of these constants at 0 GPa calculated with the GGA-PBESol approximation are depicted in Table 6 and compared to those already reported by Huang et al.,<sup>40</sup> but translated from the *Pbnm* to the *Pnma* setting for the sake of comparison. In addition to this, a comparison of our calculation with the one obtained by Fang Gu et al. in BaHfO<sub>3</sub> cubic perovskite,<sup>79</sup> whose elastic constant tensor has only three independent elastic constants, C<sub>11</sub>, C<sub>12</sub>, and C<sub>44</sub>, was carried out (see Table 6).

As observed, our calculated values with the GGA-PBESol approximation are quite similar to those calculated with the LDA approximation but not so comparable to those calculated with the GGA approximation. In any case, we have to note that the agreement between experimental and theoretical lattice parameters is rather good in our calculations (see Table 1).

The elastic constants C<sub>11</sub>, C<sub>22</sub>, and C<sub>33</sub> are associated with the deformation behavior and atomic bonding characteristics. It can be observed from Table 6 that C<sub>33</sub> > C<sub>22</sub> > C<sub>11</sub> for YAlO<sub>3</sub>, both in our calculations and in previous ones.<sup>40</sup> This result indicates that the atomic bonds between nearest neighbors along the (001) direction of the *Pnma* structure are stronger than those along the (010) and (100) directions. This agrees with the fact that the lattice constant *c* is less sensitive to pressure than the other two lattice constants (see section 4.1). The C<sub>11</sub>, C<sub>22</sub>, and C<sub>33</sub> elastic constants, which are related to the unidirectional

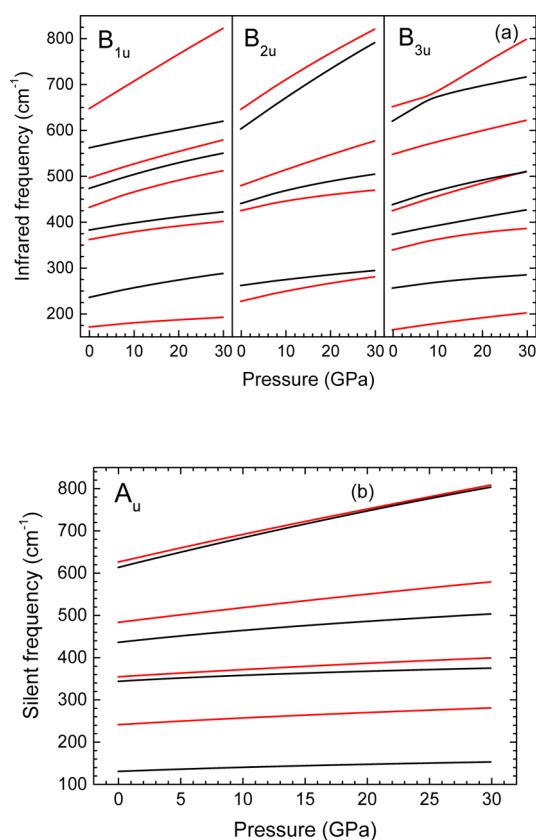


**Figure 9.** Theoretical pressure dependence of the  $B_{1u}$ ,  $B_{2u}$ , and  $B_{3u}$  infrared (a) and  $A_u$  silent (b) modes of bulk  $YAlO_3$  up to 30 GPa. Colors are given just as a guide for the eyes.

compression along the principal crystallographic directions, are larger than the  $C_{44}$ ,  $C_{55}$ , and  $C_{66}$  constants, which represent the resistance to shear deformation. This result indicates the larger resistance of  $YAlO_3$  to unidirectional compression than to shear deformation. The same behavior can be observed in  $BaHfO_3$ , since  $C_{11} > C_{44}$  (see Table 6).

When a nonzero stress is applied to the crystal, the elastic constant ( $C_{ijkl}$ ) cannot be used. Because of this, the elastic stiffness coefficients ( $B_{ijkl}$ ) must be employed instead.

In the case of hydrostatic pressure applied to an orthorhombic system, the elastic stiffness coefficients convert to  $B_{ii}$  and  $B_{jj}$  which can be calculated according to refs 80 and 81.

The elastic stiffness constants allow us to obtain the elastic properties such as the bulk modulus  $B$  and the shear modulus  $G$  of a material at any hydrostatic pressure. We calculated the shear modulus, the bulk modulus, the Young's modulus  $E$ , and the Poisson's coefficient  $\nu$  employing the Hill approximation,<sup>82</sup> which is defined as the arithmetic average of the Voigt and Reuss models.<sup>83</sup>

Another magnitude that can be estimated is the Vickers hardness ( $H_V$ ) in the Hill approximation, which is used to predict the hardness of the material.<sup>84</sup>

The theoretical values of these moduli for  $YAlO_3$  at 0 GPa are given in Table 7, in which they are also compared to those previously obtained by Huang et al.<sup>40</sup> Theoretical values of some of these elastic moduli of  $BaHfO_3$  cubic perovskite are also shown in Table 7 for comparison.

The bulk modulus is a relevant parameter related to the resistance of the material to a uniform or hydrostatic

**Table 5.** Theoretical Frequencies, Pressure Coefficients and Grüneisen Parameters of IR-Active Modes for Bulk  $YAlO_3$  up to 30 GPa<sup>a</sup>

modes	theoretical			
	$\omega_0$ ( $\text{cm}^{-1}$ )	$\partial\omega/\partial P$ ( $\text{cm}^{-1} \text{ GPa}^{-1}$ )	$\partial\omega/\partial P^2$ ( $\text{cm}^{-1} \text{ GPa}^{-2} \times 10^3$ )	$\gamma$
$B_{3u}$	163(2)	1.48(1)	-18(1)	1.86
$B_{1u}$	169(2)	0.96(2)	-19(2)	1.16
$B_{2u}$	225(2)	2.35(1)	-40(2)	2.13
$B_{1u}$	234(2)	2.22(4)	-34(3)	1.94
$B_{3u}$	254(2)	1.37(1)	-30(3)	1.10
$B_{2u}$	259(2)	1.36(2)	-20(2)	1.07
$B_{3u}$	337(2)	2.59(3)	-72(2)	1.57
$B_{1u}$	360(2)	1.84(4)	-36(2)	1.04
$B_{3u}$	371(2)	1.95(2)	-14(2)	1.07
$B_{1u}$	381(2)	1.65(1)	-24(1)	0.88
$B_{3u}$	423(2)	3.30(2)	-34(3)	1.59
$B_{2u}$	423(2)	2.26(2)	-56(3)	1.09
$B_{1u}$	430(2)	3.60(3)	-68(2)	1.71
$B_{3u}$	436(2)	3.26(2)	-62(3)	1.53
$B_{2u}$	439(2)	3.05(2)	-66(2)	1.42
$B_{1u}$	472(2)	3.29(1)	-56(2)	1.42
$B_{2u}$	478(2)	3.59(1)	-26(3)	1.54
$B_{1u}$	494(2)	3.17(1)	-30(2)	1.31
$B_{3u}$	546(2)	2.84(2)	-28(1)	1.06
$B_{1u}$	560(2)	2.09(4)	-14(2)	0.76
$B_{2u}$	602(2)	7.02(3)	-56(2)	2.38
$B_{3u}$	619(2)	5.68(3)	-181(2)	1.88
$B_{2u}$	644(2)	6.71(3)	-66(2)	2.13
$B_{1u}$	646(2)	6.11(3)	-22(2)	1.93
$B_{3u}$	650(2)	3.33(2)	112(3)	1.05

<sup>a</sup>A second-order polynomial fit was used in order to obtain the pressure dependence of the theoretical frequencies.

**Table 6.** Generalized Elastic Constants,  $C_{ij}$  (in GPa), of Bulk  $YAlO_3$  at Ambient Pressure<sup>a</sup>

$ij$	$C_{ij}$ this work	$C_{ij}$ <sup>b</sup> LDA	$C_{ij}$ <sup>b</sup> GGA	$C_{ij}$ <sup>c</sup>
11	304.0(2)	299.4	192.7	340
22	346.4(2)	330.0	285.5	
33	369.9(2)	397.0	337.0	
44	137.8(2)	158.4	140.3	72
55	102.9(2)	119.1	80.8	
66	160.4(2)	162.7	147.7	
12	134.0(2)	124.2	99.3	12
13	132.9(2)	121.7	90.4	
23	142.8(2)	140.3	136.0	

<sup>a</sup>Values of elastic constants of cubic perovskite  $BaHfO_3$  (last column) of ref 78 are also shown for comparison. <sup>b</sup>Reference 40. <sup>c</sup>Reference 79. Our values calculated with the GGA-PBESol approximation are compared to those of ref 40, translated into the  $Pnma$  setting, which used the LDA and GGA approximation.

compression. It is important to mention that the bulk modulus in the Voigt approximation,  $B_V$  (204.4(3) GPa), at 0 GPa is in good agreement with the one obtained from EOS (see Table 1). This coincidence of both results suggests the consistency of our calculations.

Another parameter that is convenient to analyze is the ratio of bulk to shear modulus  $B/G$  considering that the bulk modulus  $B$  is related to the resistance to compression, while the shear modulus  $G$  represents the resistance to plastic deformation. If  $B/G > 1.75$ , the material behaves in a ductile

Table 7. Values of Elastic Moduli at 0 GPa in Bulk  $\text{YAlO}_3$  Using Voigt, Reuss, and Hill Approximations

	$B_V$	$B_R$	$B_H$	$G_V$	$G_R$	$G_H$	$B/G$	$H_V$	$E$	$\nu$	$A_U$
this work	204.4(3)	119.3(3)	161.9(3)	120.9(3)	120.7(3)	120.8(3)	1.34(3)	19.66(3)	287(3)	0.19(1)	0.72(2)
LDA <sup>a</sup>	199.80	196.70	198.30	130.70	125.10	127.90	1.55	17.33	315.80	0.23	0.25
GGA <sup>a</sup>	163.0	150.4	156.7	106.4	95.4	100.9	1.55	14.63	249.2	0.23	0.66
GGA <sup>b</sup>			157			93	1.68		234	0.25	

<sup>a</sup>Reference 40. <sup>b</sup>Reference 79. The isotropic bulk modulus ( $B$  in GPa), shear modulus ( $G$  in GPa), and the universal anisotropy index ( $A_U$ ). Young's modulus ( $E$  in GPa), Poisson's ratio ( $\nu$ ), Vickers hardness ( $H_V$  in GPa), and ratio of bulk to shear modulus of the polycrystalline phase ( $B/G$ ) are estimated from values of Hill's approximation at 0 GPa. Our values are compared to those of ref 40 and using the LDA and GGA approximation. Comparison with the GGA approximation in  $\text{BaHfO}_3$  cubic perovskite is also given (ref 79).

way and, otherwise, in a brittle manner.<sup>85</sup> The theoretical  $B/G$  ratio for  $\text{YAlO}_3$  at 0 GPa is 1.34 (1.68 for  $\text{BaHfO}_3$ ) (see Table 7). Hence, this material is brittle at ambient pressure in agreement with previous calculations.<sup>40</sup>

Concerning the Poisson coefficient  $\nu$ , it is known that it is related to the volume change during elastic deformation.<sup>83</sup> In other words, it measures the stability of a crystal against shear. If  $\nu = 0.5$ , it means that there is no volume change during elastic deformation. In addition to this, this parameter provides more information about characteristics of the bonding forces than any other elastic modulus.<sup>83</sup> A value of  $\nu = 0.25$  supposes the lower limit for central-force solids and 0.5 corresponds to infinite elastic anisotropy.<sup>83</sup> For  $\text{YAlO}_3$ , the value  $\nu = 0.19$  suggests that the interatomic forces in this material are noncentral, whereas  $\text{BaHfO}_3$  interatomic forces are central.<sup>79</sup>

One of the most important elastic properties of crystal for both engineering and physics fields is the elastic anisotropy, because it is related to the possibility of inducing microcracks in the materials.<sup>86</sup> This property can be quantified with the universal elastic anisotropy index  $A_U$ .<sup>87</sup>

If  $A_U = 0$ , there is not anisotropy. The more this magnitude differs from 0, the more elastically anisotropic the crystalline structure. In our case,  $A_U = 0.72$  at 0 GPa; thus,  $\text{YAlO}_3$  is slightly anisotropic at ambient pressure, also in good agreement with previous calculations.<sup>40</sup>

The evolution of the  $B_{ij}$  elastic stiffness coefficients as a function of pressure (up to 95 GPa) is shown in Figure 10. It can be observed that  $B_{11}$ ,  $B_{33}$ ,  $B_{12}$ ,  $B_{13}$ , and  $B_{23}$  increase with the pressure in the whole pressure range. On the other hand,  $B_{22}$  increases notably with pressure up to 75 GPa and then increases slowly, tending to saturation from 80 GPa upward. Concerning the stiffness coefficients  $B_{44}$ ,  $B_{55}$ , and  $B_{66}$ , all of

them increase up to a certain value of pressure and then decrease dramatically, increasing the first and the second one up to 34 GPa, while the last one only up to 14 GPa, and then decreasing all of them up to 95 GPa.

It is interesting to analyze the evolution of the elastic moduli with pressure in the whole range from 0 up to 95 GPa (see Figure 11). The Hill  $B_H$  bulk modulus increases until 80 GPa, above which it decreases. On the other hand, the Hill  $G_H$  shear modulus increases until 20 GPa, and begins to decrease above this pressure, with the decrease being more noticeable in the pressure range in which the material becomes unstable ( $\sim 92$  GPa), as will be commented later.

Concerning the Young's modulus  $E$ , which is related to the stiffness of the material, it increases until 34 GPa and then decreases, being more noticeable at  $\sim 90$  GPa. This suggests that the pressure increases the hardness of the  $\text{YAlO}_3$  but also becomes less stiff with it, due to the decrease of the Young's modulus with pressure.

The Poisson coefficient  $\nu$  increases in the whole pressure range, taking a value of 0.35 before the material becomes unstable.

In the case of  $\text{BaHfO}_3$  cubic perovskite, these elastic moduli increase in the whole range of pressure up to 80 GPa, suggesting that the pressure improves the hardness and the stiffness of the material.<sup>79</sup>

Regarding the ratio of bulk to shear modulus  $B/G$ , it increases with pressure, being more noticeable near the instability pressure region, indicating that the material becomes more ductile with increasing pressure. In fact,  $\text{YAlO}_3$  presents a brittle behavior until 24 GPa and behaves as a ductile material above this pressure. Finally, the universal anisotropy index  $A_U$  increases with pressure, suggesting that the mechanical properties of this material become more anisotropic as pressure increases.

To conclude, we will analyze the mechanical stability of the orthorhombic  $Pnma$  structure of  $\text{YAlO}_3$ . It is well-known that the Born stability criteria are fulfilled when a crystal lattice is mechanically stable.<sup>80,88</sup>

Our calculated elastic constants of  $\text{YAlO}_3$  at 0 GPa satisfy these criteria, thus confirming the mechanical stability of the orthorhombic structure of the  $\text{YAlO}_3$  crystal at ambient pressure.

When a nonzero stress is applied to the crystal, the former stability criteria must be modified using the elastic stiffness coefficients instead of the elastic constants. The new condition criteria, known as the "generalized Born stability criteria", have to be considered.<sup>89</sup>

Thus, orthorhombic  $\text{YAlO}_3$  crystal is mechanically stable under hydrostatic pressure when the generalized Born stability criteria are fulfilled at once.

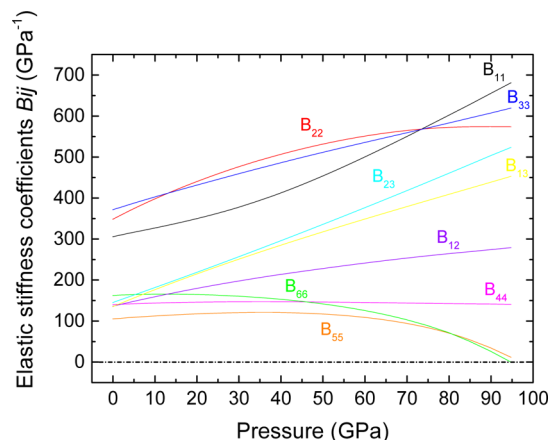
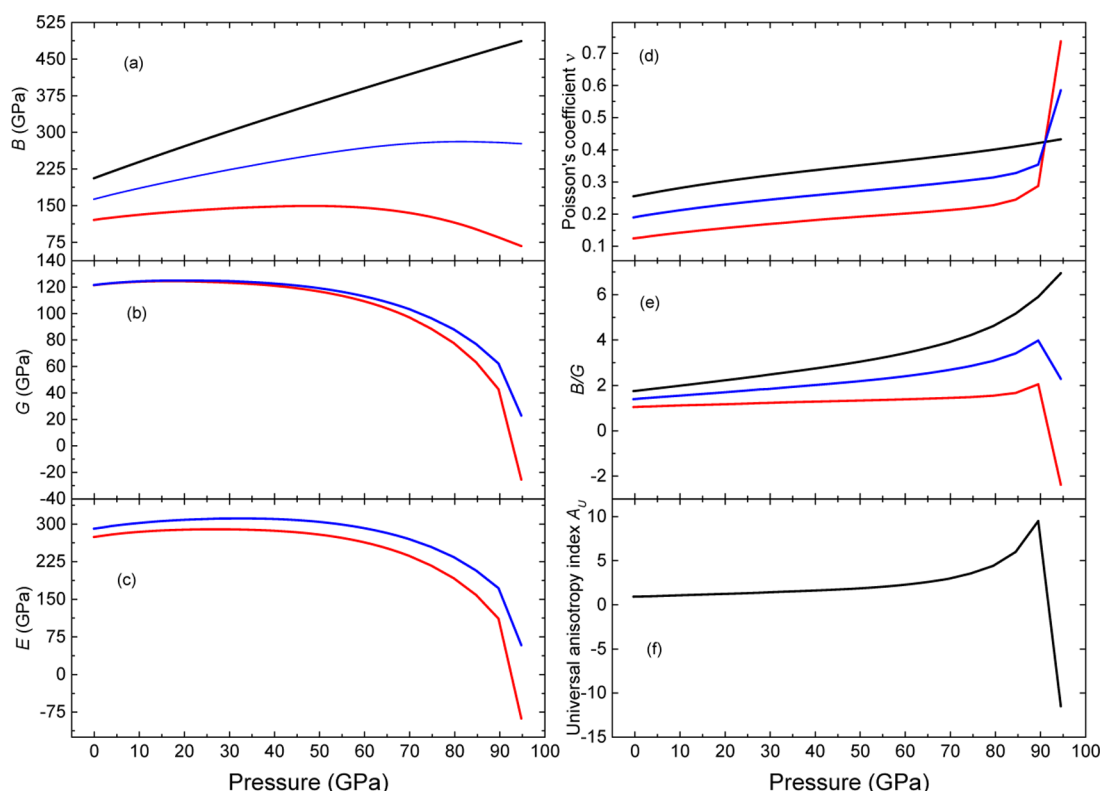


Figure 10. Evolution of the elastic stiffness constants  $B_{ij}$  as a function of pressure up to 95 GPa.





**Figure 11.** Pressure evolution up to 95 GPa of (a)  $B$ , (b)  $G$ , (c)  $E$ , (d)  $\nu$ , (e)  $B/G$ , and (f)  $A_U$  in  $\text{YAlO}_3$ . Black, red, and blue curves refer to the Voigt, Reuss, and Hill approximations, respectively.

The evolution of the generalized Born stability criteria  $M_i$  ( $i = 1-6$ ) as a function of pressure up to 95 GPa is depicted in Figure 12. It can be observed that the  $M_4 > 0$  stability criterion

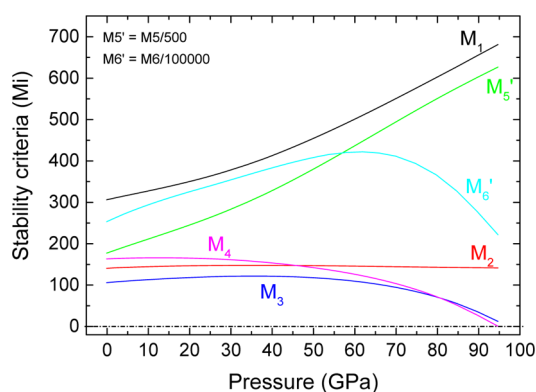


**Figure 12.** Pressure evolution of the generalized Born stability criteria up to 95 GPa.

is violated at 92 GPa and the  $M_3 > 0$  criterion is also violated at a higher pressure. These results suggest that  $\text{YAlO}_3$  becomes mechanically unstable above 92 GPa. Above this pressure, an amorphization or a phase transition could occur in  $\text{YAlO}_3$ . In the case of  $\text{BaHfO}_3$  cubic perovskite, the mechanical stability criteria are not fulfilled since 82 GPa, where the instability occurs.<sup>79</sup>

It is relevant to notice that a phase transition in  $\text{YAlO}_3$  from the orthorhombic  $Pbnm$  (or  $Pnma$ ) phase to the tetragonal  $I4/mcm$  phase has been predicted at 80 GPa.<sup>29</sup> Our calculations of enthalpy at 0 K for these two phases predict this phase transition above 100 GPa. This discrepancy between the two *ab*

*initio* calculations could be related to the use of different exchange-correlation functionals. In any case, we have shown that the low-pressure orthorhombic phase is not stable above 92 GPa, so a phase transition to the  $I4/mcm$  phase could be observed already near 92 GPa. In this respect, we have checked that the cubic perovskite  $Pm-3m$  phase, the postperovskite  $Cmcm$  phase,<sup>90</sup> the postperovskite  $Pnma$  phase of  $\text{Sb}_2\text{S}_3$  as observed in  $\text{NaFeF}_3$ ,<sup>91</sup> and the other possible phase of  $\text{YAlO}_3$  reported in the ICDS database ( $P6_3/mmc$ )<sup>90</sup> are not competitive with the tetragonal  $I4/mcm$  phase in the pressure range above 80 GPa, so the pressure-induced phase transition to the  $I4/mcm$  phase is the most probable one we have found. We want to also note that in this tetragonal phase the coordination of Al atoms is 6 with Al–O bond distances near 1.7 Å, whereas the coordination of Y atoms is already 12 with four Y–O distances near 2.17 Å, four near 2.36 Å, and other four near 2.65 Å around 100 GPa. Moreover, this HP transition is consistent with the tendency of the orthorhombic structure of  $\text{YAlO}_3$  toward a more symmetric structure on increasing pressure. Experiments of  $\text{YAlO}_3$  up to the Mbar region are needed in order to verify this phase transition.

## CONCLUSION

XRD and RS measurements of  $\text{YAlO}_3$  nanoperoovskite (with size around 40 nm) performed up to 7 and 30 GPa, respectively, have allowed us to study the experimental structural and vibrational properties of this material at HP and compare them to previously reported experimental and theoretical data of bulk  $\text{YAlO}_3$ .<sup>25,26,29</sup> Besides, our experimental results have been nicely compared to our own *ab initio* calculations, noticing that both structural parameters and vibrational modes of  $\text{YAlO}_3$  nanoperoovskite are similar to

those of bulk material. This result suggests that 40 nm size  $\text{YAlO}_3$  nanocrystals behave as bulk material. The contribution of each atom and each polyhedral unit to the different vibrational modes has been discussed. Finally, the theoretical elastic properties of this perovskite have been discussed both at ambient and at high pressure. It has been found that generalized stability conditions are violated at 92 GPa, thus suggesting that  $\text{YAlO}_3$  perovskite is mechanically stable up to 92 GPa. Consistent with theoretical calculations, no phase transition has been observed experimentally in our RS measurements up to 30 GPa. Therefore, a similar behavior is expected for  $\text{GdAlO}_3$  at high pressures. Finally, it must be mentioned that our calculations support a possible phase transition from the  $Pnma$  phase to the tetragonal  $I4/mcm$  phase in  $\text{YAlO}_3$  at pressures above 92 GPa.

## ■ ASSOCIATED CONTENT

### ● Supporting Information

The Supporting Information is available free of charge on the ACS Publications website at DOI: 10.1021/acs.jpcc.7b04245.

Typical TEM image of the  $\text{YAlO}_3$  nanoperovskite (section S1), table with the experimental lattice parameters, volume cell and refinement parameters obtained from profile matching at different pressures (section S2), table with the EOS equation state parameters for  $\text{YAlO}_3$  (section S3), description and figure with the normalized cell distortion factor with pressure  $d_{\text{norm}}(P)$  as a function of pressure of  $\text{YAlO}_3$  nanoperovskite (section S4), figure with the theoretical and experimental pressure dependence of the  $A_g$ ,  $B_{1g}$ ,  $B_{2g}$  and  $B_{3g}$  first-order Raman-active modes in bulk and nanoperovskite  $\text{YAlO}_3$ , respectively (section S5), description of elastic property equations (section S6), and references (PDF)

## ■ AUTHOR INFORMATION

### Corresponding Author

\*E-mail: miguelandreshr@gmail.com, mhernanr@ull.edu.es.

### ORCID

M. A. Hernández-Rodríguez: 0000-0003-4434-2371

J. González-Platas: 0000-0003-3339-2998

### Notes

The authors declare no competing financial interest.

## ■ ACKNOWLEDGMENTS

This research was partially supported by MINECO (MAT2013-46649-C4-2/3/4-P, MAT2015-71070-REDC, and MAT2016-75586-C4-2/3/4-P) and by EU-FEDER funds. M.A.H.-R. thanks MINECO for an FPI grant (BES-2014-068666).

## ■ REFERENCES

- (1) Kaminow, I. P.; Johnston, W. D. Quantitative Determination of Sources of the Electro-Optic Effect in  $\text{LiNbO}_3$  and  $\text{LiTaO}_3$ . *Phys. Rev.* **1967**, *160*, 519–522.
- (2) Zhu, S. Quasi-Phase-Matched Third-Harmonic Generation in a Quasi-Periodic Optical Superlattice. *Science* **1997**, *278*, 843–846.
- (3) Wojtowicz, A. J.; Drozdowski, W.; Wisniewski, D.; Lefaeur, J. L.; Galazka, Z.; Gou, Z.; Lukasiewicz, T.; Kisielewski, J. Scintillation Properties of Selected Oxide Monocrystals Activated with Ce and Pr. *Opt. Mater.* **2006**, *28*, 85–93.
- (4) Kan, D.; Terashima, T.; Kanda, R.; Masuno, A.; Tanaka, K.; Chu, S.; Kan, H.; Ishizumi, A.; Kanemitsu, Y.; Shimakawa, Y.; et al. Blue-Light Emission at Room Temperature from Ar<sup>+</sup>-Irradiated  $\text{SrTiO}_3$ . *Nat. Mater.* **2005**, *4*, 816–819.
- (5) Takashima, H.; Shimada, K.; Miura, N.; Katsumata, T.; Inaguma, Y.; Ueda, K.; Itoh, M. Low-Driving-Voltage Electroluminescence in Perovskite Films. *Adv. Mater.* **2009**, *21*, 3699–3702.
- (6) Yang, S. Y.; Seidel, J.; Byrnes, S. J.; Shafer, P.; Yang, C.-H.; Rossell, M. D.; Yu, P.; Chu, Y.-H.; Scott, J. F.; Ager, J. W.; et al. Above-Bandgap Voltages from Ferroelectric Photovoltaic Devices. *Nat. Nanotechnol.* **2010**, *5*, 143–147.
- (7) Wang, S.; Zhou, H.; Wang, X.; Pan, A. Up-Conversion Luminescence and Optical Temperature-Sensing Properties of Er<sup>3+</sup>-Doped Perovskite  $\text{Na}_{0.5}\text{Bi}_{0.5}\text{TiO}_3$  Nanocrystals. *J. Phys. Chem. Solids* **2016**, *98*, 28–31.
- (8) Du, P.; Luo, L.; Li, W.; Yue, Q. Upconversion Emission in Er-Doped and Er/Yb-Codoped Ferroelectric  $\text{Na}_{0.5}\text{Bi}_{0.5}\text{TiO}_3$  and Its Temperature Sensing Application. *J. Appl. Phys.* **2014**, *116*, 014102–014106.
- (9) Alencar, M. A. R. C.; Maciel, G. S.; De Araújo, C. B.; Patra, A. Er<sup>3+</sup>-Doped  $\text{BaTiO}_3$  Nanocrystals for Thermometry: Influence of Nanoenvironment on the Sensitivity of a Fluorescence Based Temperature Sensor. *Appl. Phys. Lett.* **2004**, *84*, 4753–4755.
- (10) Weber, M. J.; Bass, M.; Andringa, K.; Monchamp, R. R.; Comperch, E. Czochralski Growth and Properties of  $\text{YAlO}_3$  Laser Crystals. *Appl. Phys. Lett.* **1969**, *15*, 342–345.
- (11) Neuroth, G.; Wallrafen, F. Czochralski Growth and Characterisation of Pure and Doped  $\text{YAlO}_3$  Single Crystals. *J. Cryst. Growth* **1999**, *198–199*, 435–439.
- (12) Rabinovich, W. S.; Bowman, S. R.; Feldman, B. J.; Winings, M. J. Tunable Laser Pumped 3  $\mu\text{m}$  Ho:  $\text{YAlO}_3$  Laser. *IEEE J. Quantum Electron.* **1991**, *27*, 895–897.
- (13) Romero, J. J.; Montoya, E.; Bausá, L. E.; Agulló-Rueda, F.; Andreeta, M. R. B.; Hernandez, A. C. Multiwavelength Laser Action of Nd<sup>3+</sup>:  $\text{YAlO}_3$  Single Crystals Grown by the Laser Heated Pedestal Growth Method. *Opt. Mater.* **2004**, *24*, 643–650.
- (14) Fibrich, M.; Hambálek, T.; Němec, M.; Šulc, J.; Jelínková, H. Multiline Generation Capabilities of Diode-Pumped Nd: YAP and Nd: YAG Lasers. *Laser Phys.* **2014**, *24*, 035803.
- (15) Roduner, E. Size Matters: Why Nanomaterials Are Different. *Chem. Soc. Rev.* **2006**, *35*, 583–592.
- (16) Lemański, K.; Gągor, A.; Kurnatowska, M.; Pzik, R.; Dereń, P. J. Spectroscopic Properties of Nd<sup>3+</sup> Ions in Nano-Perovskite  $\text{CaTiO}_3$ . *J. Solid State Chem.* **2011**, *184*, 2713–2718.
- (17) Lemański, K.; Dereń, P. J. Spectroscopic Properties of Dy<sup>3+</sup> Ions in  $\text{CaTiO}_3$  Nano-Perovskites. *J. Lumin.* **2014**, *145*, 661–664.
- (18) Dereń, P. J.; Mahiou, R.; Pązik, R.; Lemanski, K.; Stręk, W.; Boutinaud, P. Upconversion Emission in  $\text{CaTiO}_3$ : Er<sup>3+</sup> Nanocrystals. *J. Lumin.* **2008**, *128*, 797–799.
- (19) Dereń, P. J.; Lemazski, K.; Gągor, A.; Watras, A.; Malecka, M.; Zawadzki, M. Symmetry of  $\text{LaAlO}_3$  Nanocrystals as a Function of Crystallite Size. *J. Solid State Chem.* **2010**, *183*, 2095–2100.
- (20) Lemański, K.; Dereń, P. J. Luminescent Properties of dysprosium(III) Ions in  $\text{LaAlO}_3$  Nanocrystallites. *J. Rare Earths* **2011**, *29*, 1195–1197.
- (21) Pereira, A. F.; Kumar, K. U.; Silva, W. F.; Santos, W. Q.; Jaque, D.; Jacinto, C. Yb<sup>3+</sup>/Tm<sup>3+</sup> Co-Doped  $\text{NaNbO}_3$  Nanocrystals as Three-Photon-Excited Luminescent Nanothermometers. *Sens. Actuators, B* **2015**, *213*, 65–71.
- (22) Shi, C.; Qin, H.; Zhao, M.; Wang, X.; Li, L.; Hu, J. Investigation on Electrical Transport, CO Sensing Characteristics and Mechanism for Nanocrystalline  $\text{La}_{1-x}\text{Ca}_x\text{FeO}_3$  Sensors. *Sens. Actuators, B* **2014**, *190*, 25–31.
- (23) Hu, F.; Zhang, H.; Sun, C.; Yin, C.; Lv, B.; Zhang, C.; Yu, W. W.; Wang, X.; Zhang, Y.; Xiao, M. Superior Optical Properties of Perovskite Nanocrystals as Single Photon Emitters. *ACS Nano* **2015**, *9*, 12410–12416.
- (24) Zhao, J.; Ross, N. L.; Angel, R. J.; Carpenter, M. a; Howard, C. J.; Pawlak, D. A.; Lukasiewicz, T. High-Pressure Crystallography of

Rhombohedral  $\text{PrAlO}_3$  Perovskite. *J. Phys.: Condens. Matter* **2009**, *21*, 235403–235411.

(25) Ross, N. L.; Zhao, J.; Angel, R. J. High-Pressure Single-Crystal X-Ray Diffraction Study of  $\text{YAlO}_3$  Perovskite. *J. Solid State Chem.* **2004**, *177*, 1276–1284.

(26) Ross, N. L. Distortion of  $\text{GdFeO}_3$ -Type Perovskites with Pressure: A Study of  $\text{YAlO}_3$  to 5 GPa. *Phase Transitions* **1996**, *58*, 27–41.

(27) Guennou, M.; Bouvier, P.; Garbarino, G.; Kreisel, J. Structural Investigation of  $\text{LaAlO}_3$  up to 63 GPa. *J. Phys.: Condens. Matter* **2011**, *23*, 395401–395405.

(28) Ross, N. L.; Zhao, J.; Angel, R. J. High-Pressure Structural Behavior of  $\text{GdAlO}_3$  and  $\text{GdFeO}_3$  Perovskites. *J. Solid State Chem.* **2004**, *177*, 3768–3775.

(29) Wu, X.; Qin, S.; Wu, Z. Generalized Gradient Approximation Calculations of the Pressure-Induced Phase Transition of  $\text{YAlO}_3$  Perovskite. *J. Phys.: Condens. Matter* **2006**, *18*, 3907–3916.

(30) Verma, A. K.; Modak, P. Ab-Initio Investigations of R3c to Pm3m Transition in  $\text{RAlO}_3$  (La, Pr and Nd) Perovskites under Pressure. *AIP Conf. Proc.* **2012**, *1512*, 86–87.

(31) Ross, N. L. High Pressure Study of  $\text{ScAlO}_3$  Perovskite. *Phys. Chem. Miner.* **1998**, *25*, 597–602.

(32) Magyari-Köpe, B. High-Pressure Structure of  $\text{ScAlO}_3$  Perovskite. *J. Geophys. Res.* **2002**, *107*, ECV 1-1–ECV 1-6.

(33) Bouvier, P.; Kreisel, J. Pressure-Induced Phase Transition in  $\text{LaAlO}_3$ . *J. Phys.: Condens. Matter* **2002**, *14*, 3981–3991.

(34) Kennedy, B. J.; Vogt, T.; Martin, C. D.; Parise, J. B.; Hriljac, J. A. Pressure-Induced Phase Transition in  $\text{PrAlO}_3$ . *Chem. Mater.* **2002**, *14*, 2644.

(35) Zhao, J.; Ross, N. L.; Angel, R. J. New View of the High-Pressure Behaviour of  $\text{GdFeO}_3$ -Type Perovskites. *Acta Crystallogr., Sect. B: Struct. Sci.* **2004**, *60*, 263–271.

(36) Hua, H.; Vohra, Y. K. Pressure-Induced Blueshift of  $\text{Nd}^{3+}$  Fluorescence Emission in  $\text{YAlO}_3$ : Near Infrared Pressure Sensor. *Appl. Phys. Lett.* **1997**, *71*, 2602.

(37) Barnett, J. D. An Optical Fluorescence System for Quantitative Pressure Measurement in the Diamond-Anvil Cell. *Rev. Sci. Instrum.* **1973**, *44*, 1.

(38) Zhydashchik, Y.; Galanciak, D.; Kobayakov, S.; Berkowski, M.; Kamińska, A.; Suchocki, A.; Zakharko, Y.; Durygin, A. Photoluminescence Studies of  $\text{Mn}^{4+}$  Ions in  $\text{YAlO}_3$  Crystals at Ambient and High Pressure. *J. Phys.: Condens. Matter* **2006**, *18*, 11385–11396.

(39) Bass, J. D. Elasticity of Single-Crystal  $\text{SmAlO}_3$ ,  $\text{GdAlO}_3$  and  $\text{ScAlO}_3$  Perovskites. *Phys. Earth Planet. Inter.* **1984**, *36*, 145–156.

(40) Huang, Z.; Feng, J.; Pan, W. First-Principles Calculations of Mechanical and Thermodynamic Properties of  $\text{YAlO}_3$ . *Comput. Mater. Sci.* **2011**, *50* (10), 3056–3062.

(41) Kung, J.; Rigden, S.; Gwanmesia, G. Elasticity of  $\text{ScAlO}_3$  at High Pressure. *Phys. Earth Planet. Inter.* **2000**, *118*, 65–75.

(42) Abdollahi, A.; Gholzan, S. M. Pressure-Temperature Dependence of Thermodynamic Properties of  $\text{ScAlO}_3$  Perovskite from First Principles. *Int. J. Thermophys.* **2015**, *36*, 2273–2282.

(43) Galceran, M.; Pujol, M. C.; Aguiló, M.; Díaz, F. Sol-Gel Modified Pechini Method for Obtaining Nanocrystalline  $\text{KRE}(\text{WO}_4)_2$  (RE = Gd and Yb). *J. Sol-Gel Sci. Technol.* **2007**, *42*, 79–88.

(44) Errandonea, D.; Muñoz, A.; González-Platas, J. Comment on “High-Pressure X-Ray Diffraction Study of  $\text{YBO}_3/\text{Eu}^{3+}$ ,  $\text{GdBO}_3$ , and  $\text{EuBO}_3$ : Pressure-Induced Amorphization in  $\text{GdBO}_3$ ”. *J. Appl. Phys.* **2014**, *115*, 216101–216104.

(45) Mao, H. K.; Bell, P. M.; Shaner, J. W.; Steinberg, D. J. Specific Volume Measurements of Cu, Mo, Pd, and Ag and Calibration of the Ruby R1 Fluorescence Pressure Gauge from 0.06 to 1 Mbar. *J. Appl. Phys.* **1978**, *49*, 3276–3283.

(46) Syassen, K. High Pressure Research: An Ruby Under Pressure. *High Pressure Res.* **2008**, *28*, 75–126.

(47) Hohenberg, P.; Kohn, W. Inhomogeneous Electron Gas. *Phys. Rev.* **1964**, *136*, B864–B871.

(48) Mujica, A.; Rubio, A.; Muñoz, A.; Needs, R. J. High-Pressure Phases of Group-IV, III-V, and II-VI Compounds. *Rev. Mod. Phys.* **2003**, *75*, 863–912.

(49) Kresse, G.; Furthmüller, J. Efficient Iterative Schemes for Ab Initio Total-Energy Calculations Using a Plane-Wave Basis Set. *Phys. Rev. B: Condens. Matter Mater. Phys.* **1996**, *54*, 11169–11186.

(50) Blöchl, P. E. Projector Augmented-Wave Method. *Phys. Rev. B: Condens. Matter Mater. Phys.* **1994**, *50*, 17953–17979.

(51) Perdew, J.; Ruzsinszky, A.; Csonka, G.; Vydrov, O.; Scuseria, G.; Constantin, L.; Zhou, X.; Burke, K. Restoring the Density-Gradient Expansion for Exchange in Solids and Surfaces. *Phys. Rev. Lett.* **2008**, *100*, 136406–136410.

(52) Monkhorst, H. J.; Pack, J. D. Special Points for Brillouin-Zone Integrations. *Phys. Rev. B* **1976**, *13*, 5188–5192.

(53) Nielsen, O. H.; Martin, R. M. Quantum-Mechanical Theory of Stress and Force. *Phys. Rev. B: Condens. Matter Mater. Phys.* **1985**, *32*, 3780–3791.

(54) Le Page, Y.; Saxe, P. Symmetry-General Least-Squares Extraction of Elastic Data for Strained Materials from Ab Initio Calculations of Stress. *Phys. Rev. B: Condens. Matter Mater. Phys.* **2002**, *65*, 1–14.

(55) Beckstein, O.; Klepeis, J. E.; Hart, G. L. W.; Pankratov, O. First-Principles Elastic Constants and Electronic Structure of  $\alpha\text{-Pt}_2\text{Si}$  and  $\text{PtSi}$ . *Phys. Rev. B: Condens. Matter Mater. Phys.* **2001**, *63*, 134112–134123.

(56) Parliński, K. Department of Materials Research by Computers Institute of Nuclear Physics, Polish Academy of Sciences. Computer Code Phonon. <http://wolf.ifj.edu.pl/phonon/>.

(57) Garg, A. B.; Errandonea, D.; Rodríguez-Hernández, P.; López-Moreno, S.; Muñoz, A.; Popescu, C. High-Pressure Structural Behaviour of  $\text{HoVO}_4$ : Combined XRD Experiments and Calculations Ab Initio. *J. Phys.: Condens. Matter* **2014**, *26*, 265402–265411.

(58) Sans, J. A.; Manjón, F. J.; Popescu, C.; Cuencia-Gotor, V. P.; Gomis, O.; Muñoz, A.; Rodríguez-Hernández, P.; Contreras-García, J.; Pellicer-Porres, J.; Pereira, A. L. J.; Santamaría-Pérez, D.; et al. Ordered Helium Trapping and Bonding in Compressed Arselite: Synthesis of  $\text{As}_4\text{O}_6 \bullet 2\text{He}$ . *Phys. Rev. B: Condens. Matter Mater. Phys.* **2016**, *93*, 054102–054106.

(59) Ibáñez, J.; Sans, J. A.; Popescu, C.; López-Vidrier, J.; Elvira-Betanzos, J. J.; Cuencia-Gotor, V. P.; Gomis, O.; Manjón, F. J.; Rodríguez-Hernández, P.; Muñoz, A. Structural, Vibrational, and Electronic Study of  $\text{Sb}_2\text{S}_3$  at High Pressure. *J. Phys. Chem. C* **2016**, *120*, 10547–10558.

(60) Gomis, O.; Ortiz, H. M.; Sans, J. A.; Manjón, F. J.; Santamaría-Pérez, D.; Rodríguez-Hernández, P.; Muñoz, A.  $\text{InBO}_3$  and  $\text{ScBO}_3$  at High Pressures: An Ab Initio Study of Elastic and Thermodynamic Properties. *J. Phys. Chem. Solids* **2016**, *98*, 198–208.

(61) Errandonea, D.; Mun, A.; Rodr, P.; Gomis, O.; Achary, S. N.; Popescu, C.; Patwe, S. J.; Tyagi, A. K. High-Pressure Crystal Structure, Lattice Vibrations, and Band Structure of  $\text{BiSbO}_4$ . *Inorg. Chem.* **2016**, *55*, 4958–4969.

(62) Diehl, R.; Brandt, G. Crystal Structure Refinement of  $\text{YAlO}_3$ , a Promising Laser Material. *Mater. Res. Bull.* **1975**, *10*, 85–90.

(63) Matsushita, N.; Tsuchiya, N.; Nakatsuka, K. Precipitation and Calcination Processes for Yttrium Aluminum Garnet Precursors Synthesized by the Urea Method. *J. Am. Ceram. Soc.* **1999**, *82* (8), 1977–1984.

(64) Vali, R. Vibrational, Dielectric and Scintillation Properties of  $\text{YAlO}_3$ . *J. Lumin.* **2007**, *127*, 727–730.

(65) Gonzalez-Platas, J.; Alvaro, M.; Nestola, F.; Angel, R. EosFit7-GUI: A New Graphical User Interface for Equation of State Calculations, Analyses and Teaching. *J. Appl. Crystallogr.* **2016**, *49*, 1377–1382.

(66) Sasaki, S.; Prewitt, C. T.; Liebermann, R. C. The Crystal Structure of  $\text{CaGeO}_3$  Perovskite and the Crystal Chemistry of the  $\text{GdFeO}_3$ -Type Perovskites. *Am. Mineral.* **1983**, *68*, 1189–1198.

(67) Ardit, M.; Dondi, M.; Cruciani, G. *Phys. Rev. B: Condens. Matter Mater. Phys.* **2017**, *95*, 24110–24117.



- (68) Chopelas, A. Single-Crystal Raman Spectra of  $\text{YAlO}_3$  and  $\text{GdAlO}_3$ : Comparison to Several Orthorhombic  $\text{ABO}_3$  Perovskites. *Phys. Chem. Miner.* **2011**, *38*, 709–726.
- (69) Andreasson, J.; Holmlund, J.; Rauer, R.; Käll, M.; Börjesson, L.; Knee, C. S.; Eriksson, A. K.; Eriksson, S. G.; Rübhausen, M.; Chaudhury, R. P. Electron-Phonon Interactions in Perovskites Containing Fe and Cr Studied by Raman Scattering Using Oxygen-Isotope and Cation Substitution. *Phys. Rev. B: Condens. Matter Mater. Phys.* **2008**, *78*, 1–13.
- (70) Udagawa, M.; Kohn, K.; Koshizuka, N.; Tsushima, T.; Tsushima, K. Influence of Magnetic Ordering on the Phonon Raman Spectra in  $\text{YCrO}_3$  and  $\text{GdCrO}_3$ . *Solid State Commun.* **1975**, *16*, 779–783.
- (71) Suda, J.; Kamishima, O.; Hamaoka, K.; Matsubara, I.; Hattori, T.; Sato, T. The First-Order Raman Spectra and Lattice Dynamics for  $\text{YAlO}_3$  Crystal. *J. Phys. Soc. Jpn.* **2003**, *72*, 1418–1422.
- (72) Casu, A.; Ricci, P. C.; Anedda, A. Structural Characterization of  $\text{Lu}_{0.7}\text{Y}_{0.3}\text{AlO}_3$  Single Crystal by Raman Spectroscopy. *J. Raman Spectrosc.* **2009**, *40*, 1224–1228.
- (73) Iliev, M. N.; Lee, H.-G.; Popov, V. N.; Sun, Y. Y.; Thomsen, C.; Meng, R. L.; Chu, C. W. Raman Spectroscopy of Orthorhombic Perovskitelike  $\text{YMnO}_3$  and  $\text{LaMnO}_3$ . *Phys. Rev. B: Condens. Matter Mater. Phys.* **1998**, *57*, 2872–2877.
- (74) Koshizuka, N.; Ushioda, S. Inelastic-Light-Scattering Study of Magnon Softening in  $\text{ErFeO}_3$ . *Phys. Rev. B: Condens. Matter Mater. Phys.* **1980**, *22*, 5394–5399.
- (75) Birch, F. Finite Elastic Strain of Cubic Crystals. *Phys. Rev.* **1947**, *71*, 809–824.
- (76) Monteseuro, V.; Rodríguez-Hernández, P.; Vilaplana, R.; Manjón, F. J.; Venkatramu, V.; Errandonea, D.; Lavín, V.; Muñoz, A. Lattice Dynamics Study of Nanocrystalline Yttrium Gallium Garnet at High Pressure. *J. Phys. Chem. C* **2014**, *118*, 13177–13185.
- (77) Monteseuro, V.; Rodríguez-Hernández, P.; Ortiz, H. M.; Venkatramu, V.; Manjón, F. J.; Jayasankar, C. K.; Lavín, V.; Muñoz, A. Structural, Elastic and Vibrational Properties of Nanocrystalline Lutetium Gallium Garnet under High Pressure. *Phys. Chem. Chem. Phys.* **2015**, *17*, 9454–9464.
- (78) Ross, N. L.; Zhao, J.; Burt, J. B.; Chaplin, T. D. Equations of State of  $\text{GdFeO}_3$  and  $\text{GdAlO}_3$  Perovskites. *J. Phys.: Condens. Matter* **2004**, *16*, 5721–5730.
- (79) Gu, F.; Chen, Y.; Zhang, X.; Zhang, J. First-Principles Calculations for the Structural, Elastic and Thermodynamic Properties of Cubic Perovskite  $\text{BaHfO}_3$  under Pressure. *Phys. Scr.* **2014**, *89*, 105703–105714.
- (80) Wallace, D. C. *Thermodynamics of Crystals*; Wiley: New York, 1972.
- (81) Sin'ko, G. V.; Smirnov, N. A. Ab Initio Calculations of Elastic Constants and Thermodynamic Properties of Bcc, Fcc, and Hcp Al Crystals under Pressure. *J. Phys.: Condens. Matter* **2002**, *14*, 6989–7005.
- (82) Hill, R. The Elastic Behaviour of a Crystalline Aggregate. *Proc. Phys. Soc., London, Sect. A* **1952**, *65*, 349–354.
- (83) Ravindran, P.; Fast, L.; Korzhavyi, P. A.; Johansson, B.; Wills, J.; Eriksson, O. Density Functional Theory for Calculation of Elastic Properties of Orthorhombic Crystals: Application to  $\text{TiSi}$ . *J. Appl. Phys.* **1998**, *84*, 4891–4904.
- (84) Tian, Y.; Xu, B.; Zhao, Z. Microscopic Theory of Hardness and Design of Novel Superhard Crystals. *Int. J. Refract. Hard Met.* **2012**, *33*, 93–106.
- (85) Pugh, S. F. XCII. Relations between the Elastic Moduli and the Plastic Properties of Polycrystalline Pure Metals. *London, Edinburgh, Dublin Philos. Mag. J. Sci.* **1954**, *45*, 823–843.
- (86) Tvergaard, V.; Hutchinson, J. W. Microcracking in Ceramics Induced by Thermal Expansion or Elastic Anisotropy. *J. Am. Ceram. Soc.* **1988**, *71*, 157–166.
- (87) Ranganathan, S. I.; Ostoja-Starzewski, M. Universal Elastic Anisotropy Index. *Phys. Rev. Lett.* **2008**, *101*, 55504–55507.
- (88) Born, M.; Huang, K. *Dynamical Theory of Crystal Lattices*; Oxford University Press: Oxford, U.K., 1954.
- (89) Wang, J.; Yip, S.; Phillpot, S. R.; Wolf, D. Crystal Instabilities at Finite Strain. *Phys. Rev. Lett.* **1993**, *71*, 4182–4185.
- (90) Bertaut, E. F.; Mareschal, J. Un Nouveau Type de Structure Hexagonale:  $\text{AlTO}_3$  ( $T = \text{Y, Eu, Gd, Tb, Dy, Ho, Er}$ ). *C. R. Acad. Sci.* **1963**, *257*, 867–870.
- (91) Crichton, W. A.; Bernal, F. L.; Guignard, J.; Hanfland, M.; Margadonna, S. Observation of  $\text{Sb}_2\text{S}_3$ -Type Post-Post Perovskite in  $\text{NaFe}_3$ . Implications for  $\text{ABX}_3$  and  $\text{A}_2\text{X}_3$  Systems at Ultrahigh Pressure. *Mineral. Mag.* **2016**, *80*, 659–674.